applied nano

MDPI

Review

Gas-Phase Synthesis of Functional Nanomaterials

Vladimir N. Popok [1,*] and Ondřej Kylián [2]

[1] Department of Materials and Production, Aalborg University, 9220 Aalborg, Denmark
[2] Department of Macromolecular Physics, Faculty of Mathematics and Physics, Charles University, 180 00 Prague, Czech Republic; Ondrej.Kylian@mff.cuni.cz
* Correspondence: vp@mp.aau.dk; Tel.: +45-9940-9229

Received: 31 August 2020; Accepted: 29 September 2020; Published: 2 October 2020

Abstract: Nanoparticles (NPs) of different types, especially those of metals and metal oxides, are widely used in research and industry for a variety of applications utilising their unique physical and chemical properties. In this article, the focus is put on the fabrication of nanomaterials by means of gas-phase aggregation, also known as the cluster beam technique. A short overview of the history of cluster sources development emphasising the main milestones is presented followed by the description of different regimes of cluster-surface interaction, namely, soft-landing, pinning, sputtering and implantation. The key phenomena and effects for every regime are discussed. The review is continued by the sections describing applications of nanomaterials produced by gas aggregation. These parts critically analyse the pros and cons of the cluster beam approach for catalysis, formation of ferromagnetic and superparamagnetic NPs, applications in sensor and detection technologies as well as the synthesis of coatings and composite films containing NPs in research and industrial applications covering a number of different areas, such as electronics, tribology, biology and medicine. At the end, the current state of the knowledge on the synthesis of nanomaterials using gas aggregation is summarised and the strategies towards industrial applications are outlined.

Keywords: gas-phase synthesis of nanoparticles; cluster sources; nanomaterials prepared by gas aggregation

1. Introduction

The fast-growing field of nanotechnology utilises nanoparticles (NPs) as building blocks for ultra-small systems and nanostructured materials with required, quite often unique, functionality [1–5]. Within a wide spectrum of chemical and physical methods used for NP synthesis, the gas-phase aggregation technologies have reached maturity at the research level, which makes them promising to be transferred to the industrial scale in the coming years [6,7].

Gas aggregation of atoms and molecules is a well-known naturally-occurring phenomenon. The examples are clouds or smoking fires. The condensation requires the lowering of temperature and precursors/germs. These conditions can be created artificially in gas aggregation sources enabling the formation of aggregates of atoms or molecules, so-called clusters [8]. When reaching a size of over several tens of constituents, the cluster dimensions reach the nanometre scale and they are often called nanoparticles. Therefore, in this review words "cluster" and "nanoparticle" are used as synonyms.

We can look back in time and find some single instances for the use of gas aggregation in thin film formation even 90 years ago [9]. In the 1950s and 1960s, the first experiments with small gas clusters were carried out and the concept of electrospray source was introduced [10–13]. In the 1970s, an idea similar to electrospraying was applied for the formation of cluster ion beams of metals, mostly of those with low melting point (Li, Cs, Sn, Ga and Hg); so-called liquid metal sources were developed [14–16]. The first cluster sources based on the adiabatic cooling of expanded gas in supersonic jets [17] and

on the gas aggregation of vaporized solids (metals and semiconductors) were also constructed in the 1970s [18,19]. A range of new gas aggregation techniques for cluster formation was developed throughout the 1980s. For instance, laser ablation allowed the extension of cluster production over materials with a high melting point [20,21]. This method led to the discovery of fullerenes [22]. The ion sputtering method was adopted for the production of small clusters [23]. The idea to use arc discharge for cluster formation was introduced [24], which later led to the development of the so-called microplasma source [25]. An important step in the cluster source history was the development of the magnetron sputter discharge technique, which has been known for a long time and used in thin film formation [26], towards NP production at the beginning of the 1990s [27]. Currently, magnetron sputtering cluster sources are among the most popular ones. They are available from a number of commercial suppliers in different configurations and allow for the formation of NPs of different species, structures and geometries [6,7,28,29]. From the 1990s to the 2010s, the gas aggregation cluster techniques have undergone substantial progress due to the high relevance of the rapidly developing nanoscience research [4–7,30–38]. However, to be used in the industry, sources with high deposition rate enabling mass production of NPs are required. One of the recent inventions in this direction is a source based on the assembly of atoms in a metal-loaded cryogenically-cooled rare gas matrix initiated by ion beam impact [39]. A production of ~10 mg of clusters (Au_{100}) per hour has been demonstrated [40].

From the application point of view, the formation of NPs by gas-phase aggregation provides several advantages. Since the clusters are produced in a vacuum from ultra-pure targets, this method allows very good control of composition. The gas-phase synthesis is not limited to homoatomic clusters but allows production of compound NPs, for example metal-oxide ones [28]. Such NPs may be fabricated either by adding a small amount of oxygen into the inert working gas [41,42] or by in-flight oxidation of metal clusters using an auxiliary oxygen-containing plasma before they reach the substrate [43]. Furthermore, recent studies showed that the gas aggregation sources may also be employed for the synthesis of alloy and compound NPs with tuneable shape and structure (spheres, cubes, Janus- and dumbbell NPs, as well as core@shell, multi-core@shell or core@satellite ones) [7,28,44–55]. Adding a mass-filtering system after the gas aggregation stage gives the possibility of carrying out size selection [35,56]. Varying the kinetic energy allows adjusting the cluster-surface interaction mechanism [36,57]. In the cluster sources, NPs are typically collimated into beams. Then, by scanning and varying the exposure time one can control the surface coverage or volume filling factor of clusters [32,58,59] as well as form areas with a gradient in particle density or carry out patterning through masks [35,60–62].

2. Cluster-Surface Interaction Regimes

Cluster-surface interaction can be considered of either low- or high-energy. In the low-energy regime, which is often called soft-landing, the kinetic energy per atom E_{at} is below the binding (cohesive) energy of the cluster constituents. The typical limit of E_{at} for this regime is below one eV. Under such impact conditions, the composition of deposited NPs is preserved but their structure and shape can undergo distortions and deformations.

With the kinetic energy increase, one can approach or slightly overcome the binding energy value. In this case, the energy locally transferred to the substrate can be enough to produce small radiation damage and the NP can become trapped. Such energy regime is called pinning.

Further increase of the kinetic energy leads to an energetic impact: the cluster fragments and the constituents become back-scattered or implanted.

Understanding physics and effects occurring under the above-mentioned regimes plays a crucial role in the rational design of nanoparticle-based materials with appropriate functionality. The main issues for every regime are briefly overviewed below while for a more comprehensive description the interested reader should refer to [57].

2.1. Soft-Landing

The simplest scenario of NP soft-landing may be described by the ballistic-aggregation model, in which the addition of particles to a growing structure occurs via randomly selected linear trajectories [63]. This model, originally developed for the explanation of the structure of colloidal aggregates [64,65], assumes that the arriving particle stays at the place of impact and does not move, at least at the time scale of the new particle arrival at a neighbouring site. This results in the formation of a randomly arranged array of NPs on a substrate material that for the higher fluence transforms into a stacked nanoparticle film shown in Figure 1a. Such mesoporous aggregates have densities as low as about one-half of the corresponding bulk materials densities with functional properties given by the properties of original free clusters that are preserved upon soft-landing. Based on the numerical models, the growth of nanoparticle arrays in this deposition mode is characterised by the universal scaling law:

$$R \sim t^{\beta}, \tag{1}$$

where t is the thickness of the deposit, R is its roughness, and β stands for the growth factor that reaches value of 0.33 in the case of ballistic deposition [66,67]. Naturally, β has to be understood as the value that describes the idealised ballistic-aggregation growth of layers that does not account for the size distribution of incoming NPs, their sticking behaviour or scattering [68]. Despite slight deviations, experimentally determined values of β were found to be independent of the composition of deposited NPs and match well the theoretical value [5,69]. This is of great significance for the practical use as it paves the way for the tailor-made production of nanostructured coatings whose surface roughness may be precisely tuned by the NP fluence.

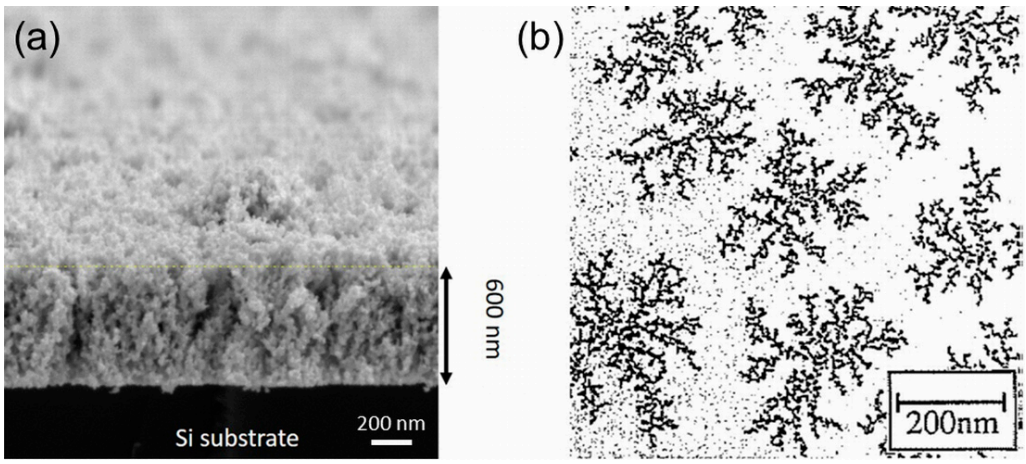

Figure 1. (**a**) Scanning electron microscopy (SEM) image of the cross-section of 600 nm thick film of soft-landed Au NPs. (**b**) Transmission electron microscopy (TEM) micrograph of a 0.5 nm thick antimony film prepared by Sb_{2300} (diameter about 5 nm) cluster deposition on graphite at room temperature. Panel (**b**) is reprinted from [70] with permission from Elsevier.

Obviously, the applicability of the ballistic-aggregation growth model is limited to the cases when the NPs may be considered as immobile after they reach the substrate or growing film. This is, in general, true for particles of a larger mass, transition metal clusters like Co or Fe [34] or in the later stages of the nanoparticle film growth when the new arriving clusters fall on already deposited ones. These become irreversibly immobilized either due to sticking between the NPs or due to the existence of a barrier that prevents them from falling down onto the substrate. However, as proved in numerous studies, even relatively large clusters composed of thousands of atoms may diffuse relatively quickly on a substrate at speeds that are in some cases comparable with those of the surface diffusion of single atoms [70–72]. Based on the experimental and theoretical studies it is believed that the cluster moves on a surface due to a collective mechanism and, thus, diffuses as a rigid structure in a similar

manner as a single atom. According to the molecular dynamics (MD) simulations, cluster movement is a combination of its rotation and translation induced by the mismatch of lattice parameters of a substrate and cluster [72,73]. Although the exact mechanism of the diffusion of NPs is still under debate, it strongly depends on the strength of substrate-cluster interaction, temperature or presence of surface defects or steps. In general, the high mobility of NPs was observed on weakly interacting substrates such as highly-oriented pyrolytic graphite (HOPG). The ability of NPs to move on a substrate results in a formation of ramified aggregates (for an example, see Figure 1b), which may be explained by the deposition–diffusion–aggregation (DDA) model. It assumes that a diffusing cluster may either encounter another diffusing NP that leads to the emergence of a new immobile "island" (nucleation event) or might be captured by already existing "island" (growth event) [74]. The actual number and appearance of growing nanostructures are then given by the combination of the particle flux towards the substrate (i.e., deposition rate) and the diffusion coefficient of individual particles.

In the aforementioned description of the DDA model so far only a juxtaposition of colliding particles was taken into the account, i.e., the individual NPs that form an aggregated nanostructure preserve their size and structure. This scenario is, however, in many cases not realistic as the colliding NPs may fully or partially coalesce. This process may be, according to a recent review [75], divided into three consecutive phases: (i) initial contact and formation of an interface between individual NPs; (ii) restructuralization/deformation of NPs supported by the heat release connected with the lowering of the free surface area of interacting NPs [76,77]; and (iii) sphericization induced by thermal diffusion of surface atoms. Naturally, the coalescence process and its rate are strongly dependent on the properties of interacting particles (e.g., their composition, size ratio, shape, crystallinity, the relative orientation between them, degree of order/disorder), temperature as well as on the substrate properties [78]. Depending on these parameters, different final structures of sintered NPs may be observed that range from structures with small neck formed between two clusters, dumbbell-like and ovoid structures to spheres [75].

The possibility of diffusing clusters to coalesce upon mutual contact naturally affects the shape of formed aggregates. A well-known example of this is the variation of the structure of created nanoislands observed in [79] for antimony clusters deposited onto graphite surface that changes from the fractal-like structure to compact islands of spherical shapes as the size of primeval Sb decreases from 500 atoms down to four atoms (Figure 2). Moreover, as the mobility of diffusing NPs is substantially influenced by the surface defects [80–83], the morphology and position of formed nanostructures may be at some extend controlled by the pre-treatment or pre-patterning of the substrate. For instance, it was shown that bends formed on a graphite surface may act as guides for aggregation of Ag_n clusters [84]: while concave bends were found to force clusters to linearly aggregate along the bend, the convex bends behave as repulsive barriers for the particle diffusion that makes it possible to laterally constrain the aggregation in variable extent including the case of quasi-one-dimensional assembly of clusters (see Figure 3a). Another example represents HOPG functionalised by a focused ion beam (FIB) prior to the deposition of clusters. As shown in [85–88], this opens the possibility to fabricate ordered arrays of aggregated NPs (see Figure 3b). Recently, such ordered silver NP patterns have been shown for the FIB-treated graphene [89]. The possibility of Cu_n clusters ordering was reported for the nanorippled Si templates using glancing angle deposition [90]. Finally, it was also suggested to use soft-landed clusters to visualise step edges, grains boundaries, grains orientation or elastic strain fields on HOPG surfaces that are all invisible by SEM [91].

In addition to previously described growth modes, the self-aggregation of clusters into ordered arrays with no mutual contact of individual clusters was reported for gold [92], platinum [92–94], and CoPt [95] clusters. Absence or presence of contact between clusters was found to be dependent on the base pressure during the deposition, size, and reactivity of NPs. For small clusters and deposition pressures above a critical value, surface reactions (e.g., CO adsorption on Pt_n clusters) modify the surface of clusters and such formed interfacial layer represents an effective repulsive barrier that obstructs the contact between individual particles (Figure 4) [92]. Additionally, this effect may even be

promoted by the deformation of the substrate surface induced by small Pt_n clusters that may explain the occurrence of arrays of non-contacting Pt_n clusters observed under ultra-high vacuum (UHV) deposition [94].

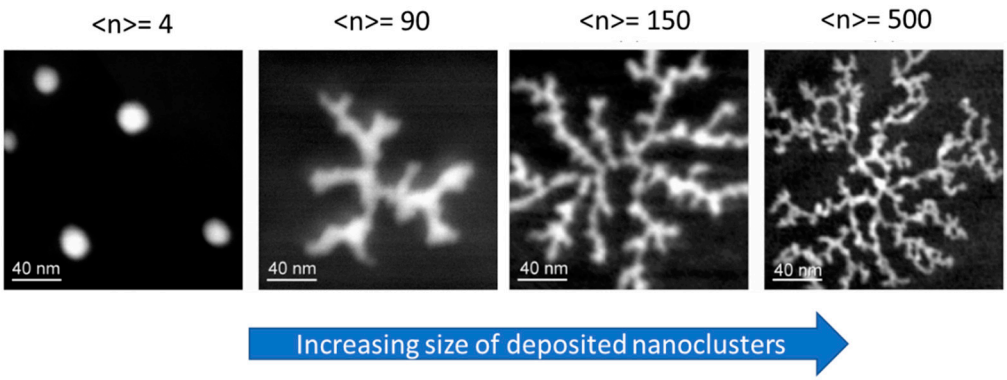

Figure 2. TEM images of antimony islands grown on graphite surfaces for different sizes of the incident clusters. Reprinted from [79] with permission from Elsevier.

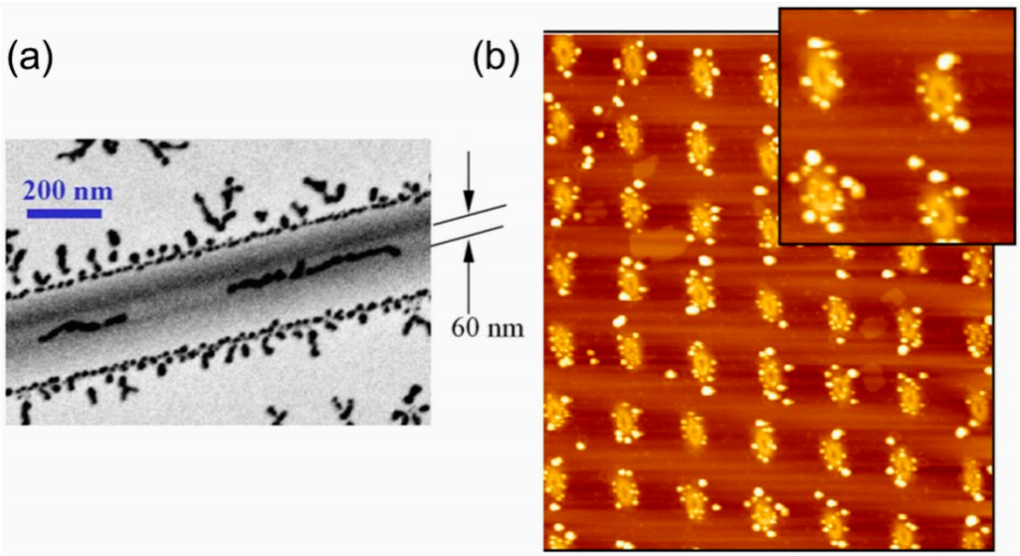

Figure 3. (**a**) Graphite pleats with three faces and two monolayers of silver cluster deposition. The fractal growth on the top face is restricted by the repulsive, convex bends between the faces of the pleat. The silver islands are forced to grow linearly and unbranched (reprinted from [84] with permission from APS). (**b**) Atomic force microscopy (AFM) images showing the morphologies of 0.05 nm thick gold-cluster films deposited on FIB-patterned HOPG substrates at 400 K (reprinted from open-access source [85]).

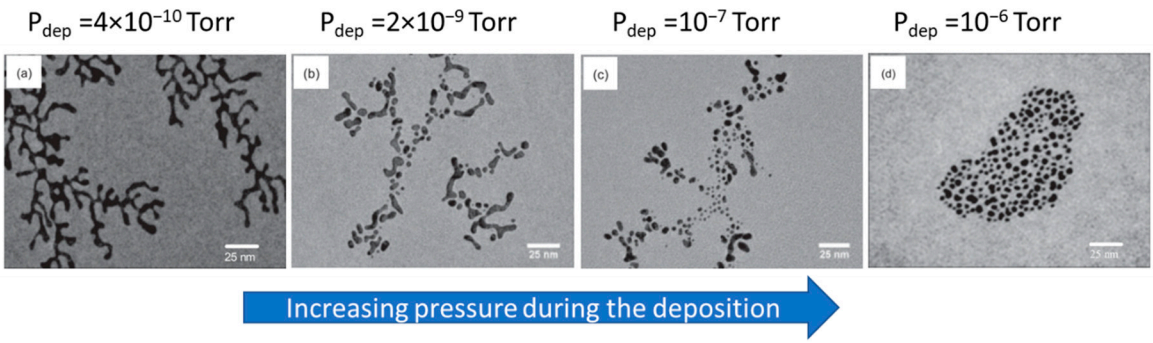

Figure 4. Effect of the pressure (P_{dep}) during the deposition of the size-selected gold clusters (2 nm in diameter) on island morphologies. Reprinted from [92] with permission from APS.

The small NPs can, in addition, undergo important structural (rearrangement of cluster constituents) and morphological (mainly flattening) changes when in contact with a substrate [96–98]. This is due to the dominant role of cluster-surface interaction with decreasing the size of deposited particles. The degree of such changes is dependent on the surface and interface energies as well as on the binding energies of cluster constituents. For instance, according to MD simulation of Au_{440} cluster deposited onto an Au(111) substrate, the complete epitaxy is achieved within 100 ps, as shown in Figure 5. At this point, it has to be stressed that the largest cluster size leading to full contact epitaxy upon deposition decreases rapidly with the decreasing temperature. To give an example, Cu NPs deposited onto Cu substrate at room temperature reached full epitaxy only when they are composed of less than approximately 200 atoms [99]. Due to this, larger NPs remain in a non-epitaxial configuration at room temperature, although the atomic planes in the vicinity of a substrate may become epitaxial with it.

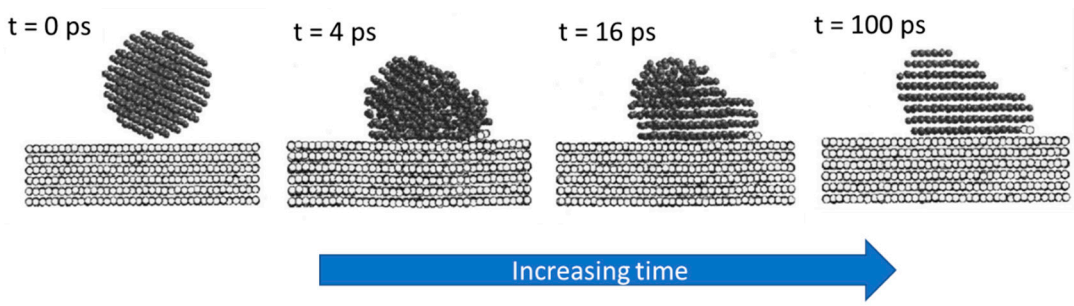

Figure 5. Snapshots of the deposition of an Au_{440} cluster on an Au(111) surface. Reprinted from [96] with permission from APS.

For completeness, it is worth mentioning that clusters may even be rebounded from the surface at relatively low impact kinetic energy. This effect, which was reported for clusters that undergo plastic deformation on impact [100], is highly sensitive on the strength of cluster-surface attraction *C*. As shown by MD simulations, the transition between adhesion and reflection of nanocluster occurs as the ratio of the kinetic energy to the adhesion energy (so-called Weber number) passes through unity [101]. From the practical point of view, changing the actual value of *C* (e.g., by exposure of a substrate to electron beam) enables to control the adhesion/reflection of nanoclusters on different positions on a substrate even at the nanometer level. This, in turn, allows for the production of well-defined patterns of clusters needed for the fabrication of functional nanodevices [100,102]. An example of this is depicted in Figure 6, where the SEM image of Bi cluster-assembled wire with an average width of ~50 nm, supported on a SiO_2 passivated Si substrate, is presented.

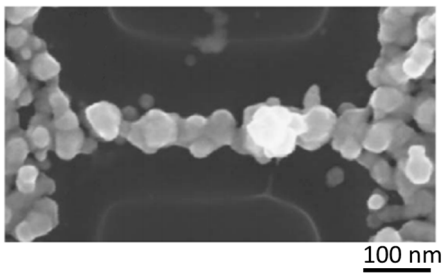

Figure 6. SEM image of Bi cluster-assembled wire supported on a SiO_2 passivated Si substrate. Reprinted from [100] with permission from AIP.

2.2. Pinning

The increase of the kinetic energy on interaction with a surface can cause deformation of the cluster shape and even a partial fragmentation if this energy approaches the binding energy of the cluster constituents. At the same time, the energy transfer to the substrate can lead to point defect

formation and the cluster can become trapped [103]. This type of interaction is called pinning because it causes surface immobilization of the cluster. Pinning of various metal clusters (Ag_n, Au_n, Pd_n, Ni_n and Co_n) is mostly studied on HOPG due to atomically flat surface [103–108]. Modelling of the metal cluster interaction showed that the energy required for the carbon recoil production E_r is approximately 5–6 eV [108,109]. Thus, above this threshold value, one can expect the cluster pinning to occur. But it was also found that the pinning energy E_{pin} depends on cluster species, size and substrate material. The following empirical equation was suggested [109]:

$$E_{pin} = \frac{nmE_r}{4NM}, \tag{2}$$

where n is the number of atoms in the cluster, m is the atomic mass of the cluster constituents, N is the number of recoil atoms and M is the atomic mass of the target.

The minimal energies required for pinning have the same order of magnitude with the cohesive energies of metal clusters. Hence, one can expect that a cluster can remain intact or may just partly fragment under the pinning regime. However, as found by MD simulations and confirmed by scanning tunnelling microscopy (STM), the resulting cluster shape significantly depends on species; Ni_n clusters are more compact, while Ag_n and Au_n clusters have tendencies to spread out forming flat structures on pinning [110]. In Figure 7, one can see that Co_n clusters follow the same tendency as Ag_n and Au_n, forming a flat island with a few atoms penetrating beneath the top graphene layer. The STM experiments revealed the formation of one atomic-layer-thick small cobalt islands at the places of impact [107], thus, supporting the modelling.

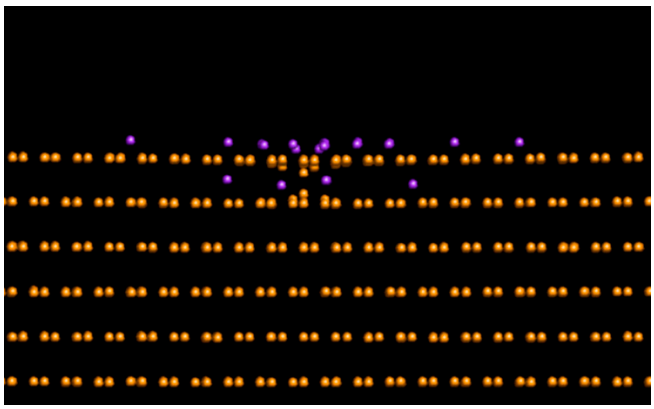

Figure 7. MD simulation, viewed in cross-section, of Co_{30} cluster 2 ps after the impact with the energy of 300 eV/cluster (10 eV/atom) on graphite.

One of the interesting consequences of metal cluster pinning to graphite is the possibility of nanoscale etching. It was found that the annealing at temperatures 600–650 °C in ambient atmosphere leads to the formation of the pits at the cluster location [108,111]. These pits typically have a hexagonal or circular shape (see Figure 8a) that is assigned to the local oxidative etching of the damaged on impact areas. Depth of the pits correlates well with the depth of radiation damage caused by the cluster impact [108,111,112]. To attack the underlying pristine graphene planes the etching time must be significantly increased. For the pinned Co_n clusters it was also found that the heating can cause worm-like planar trenches as can be seen in Figure 8b [107]. High temperature increases diffusive mobility of the residual clusters and, at the same time, they can serve as catalyst particles promoting reactions of atmospheric oxygen with carbon as schematically illustrated in Figure 9. The heating induced channelling of graphite and graphene by NPs deposited by other than gas aggregation techniques has been also reported and even suggested as a "catalytic pen" method for high-precision lithography [113–115]. However, it does not seem that there is an easy way to control the direction of particle motion and, therefore, this approach has not received any further development.

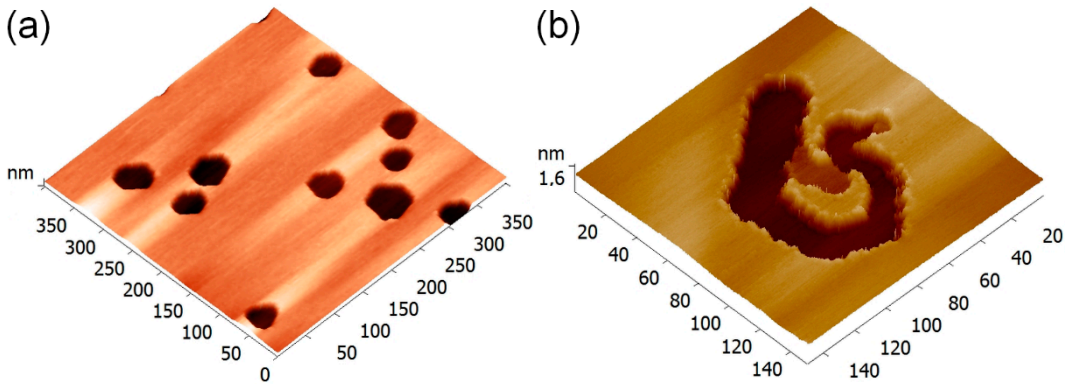

Figure 8. STM images of graphite after the impact of (**a**) Co_{63} clusters with the energy of 130 eV/atom (depth of pits ca. 3.5 nm) and (**b**) Co_{50} cluster with the energy of 12 eV/atom (channel depth is 1 (lighter) and 2 (darker) graphene layers). In both cases, the samples underwent thermal-induced etching (600 °C, 3 min in the ambient atmosphere).

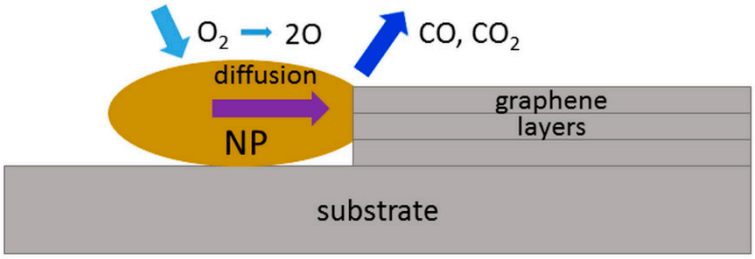

Figure 9. Schematic picture of a NP making a trench in graphite/graphene by diffusing and catalysing the reaction of atmospheric oxygen with carbon atoms.

2.3. Sputtering and Implantation

The energetic collision of an ion with atoms of a target can cause a knock-on effect leading to either sputtering of the atom or forming a recoil, which moves inside the target producing a displacement cascade [116,117]; even a small crater can form [118,119]. Crater formation was found to be a much more pronounced phenomenon for a cluster impact where the multiple collision (almost simultaneous interaction of many cluster constituents with a number of target atoms) leads to a high-energy transfer very locally. At the central part of the collision area a depression is formed while the atoms from the periphery of the impact area possess momenta directed away from the surface (see Figure 10a) [120]. These atoms either become sputtered or produce an atomistic flow leading to the rim formation (see Figure 10b). The crater parameters depend on the cluster size and energy as well as on the properties of a target. A variety of different target materials and cluster species have been studied both theoretically and experimentally [121–131]. The generally-found tendency is that the materials with higher density and melting point are less favourable for the crater formation. One of the examples is diamond [132]. Another allotropic form of carbon, graphite, responds to the cluster impacts very elastically. As shown by the MD simulations, the crater can be formed at the initial stage of impact but then the graphene sheet oscillations cause its closure [133].

Along with craters, hillocks (nm-scale protrusions, typically of cone-like shape) are often observed [123,134,135]. The MD simulations of keV-energy cluster impact predict compression of the material up to GPa level leading to temperature rise up to a few thousand degrees [120,136]. This temperature level is above a melting point for any material. The molten matter can be pushed out and quenched forming a hillock. The origin for the expulsion can be the difference in density or tension between the hot melt and the surrounding solid as well as an elastic rebound of the bulk because of the initial compression and shock wave formation. In some cases, a hillock can appear in a centre of a crater (see Figure 11) as, for example, found for the Ar_n cluster impact on silicon and sapphire [128]. By analogy with meteorite impact craters on a planet surface, where a centrally-located bump is often

seen [137], these structures are called complex craters. For more details about crater formation on cluster impact, one can refer to [37].

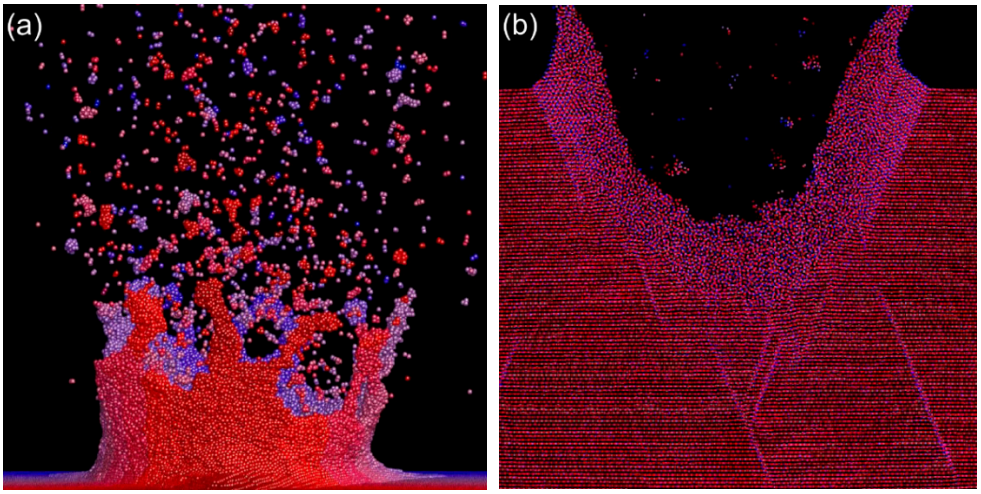

Figure 10. Snapshots of MD simulations of 650 eV Au_{13} cluster collision with a gold target: (**a**) sputtering of atoms at the beginning of the collision and (**b**) crater formation after 16 ps. Reprinted from [37] with permission from Elsevier.

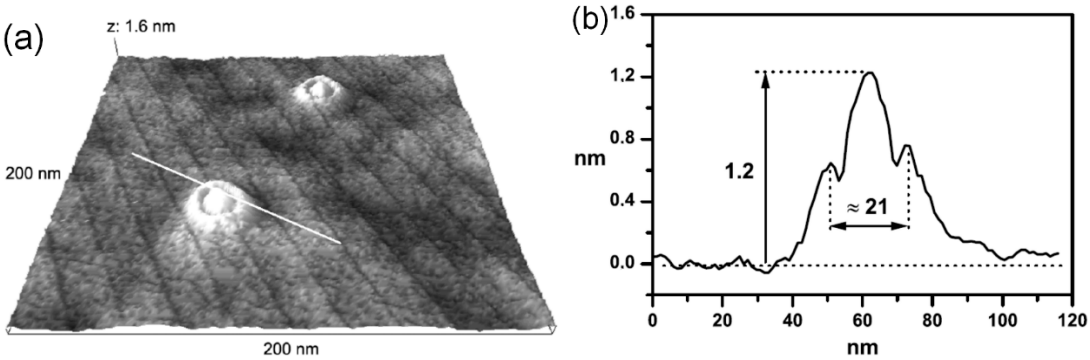

Figure 11. (**a**) AFM image of complex craters formed on the surface of silicon after 18 keV Ar_{12}^{+} cluster impact and (**b**) cross-sectional profile of one of the craters. Reprinted from [128] with permission from Springer.

As mentioned above, many target atoms get momenta directed away from the surface on the cluster impact, i.e., provide a very pronounced lateral effect. Even at normal to the surface incidence, the distribution of the sputtered atoms has a strong angular dependence and the sputtering yield Y does not follow so-called cosine law with respect to the emission angle of the atoms Θ, $Y(\Theta) \sim \cos^m\Theta$ with $m \geq 1$, which is typical for monomers [138]. Recent studies of the Cu and Mo sputtering by argon clusters have shown an anisotropy of atom distribution over azimuthal angle, which is found to be related to the crystal orientation and cluster size [139]. The use of clusters increases Y from a few atoms typical for monatomic ions to tens and even hundreds [140] making the cluster beams to be an efficient tool for sputtering and smoothing of surfaces [141]. Additional advantages of cluster sputtering in comparison with ion or plasma assisted processing are short-range damage, high spatial resolution and elimination of charge accumulation on the surface. These properties promoted the utilization of cluster ion beams in the field of secondary ion mass spectroscopy (SIMS), especially in application to organic materials [142,143]. The C_{60}^{+} and Ar_n^{+} cluster ion beams have been primarily used providing not only depth profiling of the organic species but also imaging of biological tissues [144–147].

Since clusters generate multiple collisions with target atoms on impact, the physics of cluster implantation has several fundamental differences compared to a monatomic bombardment. At the

beginning of impact, the cluster kinetic energy and momentum are locally transferred to the target causing a compression up to GPa level and rapid heating up to 10,000–100,000 K [120,123,136]. The pressure and temperature rise lead to the development of shock waves and significant thermal spikes. The latter can cause local material melting along the cluster path [148]. Under typical implantation conditions, the kinetic energy per cluster constituent is considerably higher than the cluster cohesive energy. The aggregate becomes broken on impact and the penetrating into the target constituents form collision cascades of a complex nature due to the non-linear effects originated by the interaction of these cluster constituents not only with the target atoms but also with each other. One of the closely related phenomena is the so-called clearing-the-way leading to deeper implantation of the cluster atoms compared to the monatomic projectiles with the same incident velocity [149,150]. It is explained by pushing the target atoms by the "front" cluster constituents out of the way of the cluster "rest", thus, reducing the total stopping power. The clusters composed of heavy elements cause more clearing of "light" targets and, contrarily, the effect is negligible if the cluster consists of light atoms but the target is represented by heavy elements [151]. This phenomenon is well illustrated by metal cluster implantation into polymers. It was found that small (ca. 2.7 nm in diameter) Pd NPs impacting poly(methyl methacrylate) (PMMA) with the energy of only 0.5 eV/atom become dispersed to the depth of 50 nm [152]. The clusters also stay intact because the kinetic energy per atom is below the cohesive cluster energy. Such deep penetration cannot be explained exclusively by the clearing-the-way effect. Using MD simulations, it was suggested that the local thermal and pressure spike generated by the collision facilitate cluster embedding due to an increase of chain mobility [153]. This approach on shallow implantation of metal clusters into polymers paves a way for the formation of composite films with tuneable properties towards diverse applications, which will be addressed in Section 3.4.

An important issue for cluster implantation is the prediction of the projected range, R_p. This problem was successfully solved for monatomic ions using the binary collision approach. Nowadays, well-developed and experimentally verified simulation codes exist, for example, SRIM or TRIDYN [154,155]. However, due to the complexity of the cluster-matter interaction, the simulations of cluster implantation show diversity in scaling laws with respect to energy $R_\mathrm{p} \sim E^{1/3}$ and $E^{1/2}$ [156,157] as well as to cluster size (number of atoms) $\sim n^{\alpha}$ where α ranges between 0.31 and 0.45 [157,158]. Unfortunately, it is difficult to conclude about the correctness of the suggested laws because the experimental data on systematic measurements of R_p are rather limited, except the cluster implantation into graphite.

The specificity of graphite is in its layered structure with weak Van der Waals bonds between individual graphene sheets but strong covalent bonds in the planes. The implanted cluster creates damage, amorphizing the material along the track to a certain depth. The volumes of amorphous carbon created by individual cluster impacts can be etched by short-term heating in the presence of oxygen forming pits as described in Section 2.2 (see Figure 8a). Using AFM or STM one can find the depth of radiation damage as a function of implantation energy. For not too high energies (keV scale), this depth corresponds well to R_p [132,133]. The experiments with different cluster species implanted into HOPG allowed to combine the scaling laws for energy and cluster size (mass) using the cluster momentum p, which is linearly proportional to the mass, and the velocity be a square root function of energy ($E^{1/2}$). This approach led to a new universal scaling law $R_\mathrm{p} \sim p$ proved for a wide range of cluster species and energies (see Figure 12) [108,111,133,159]. A similar dependence was also found for the keV-energy argon cluster ions implanted in diamond [160].

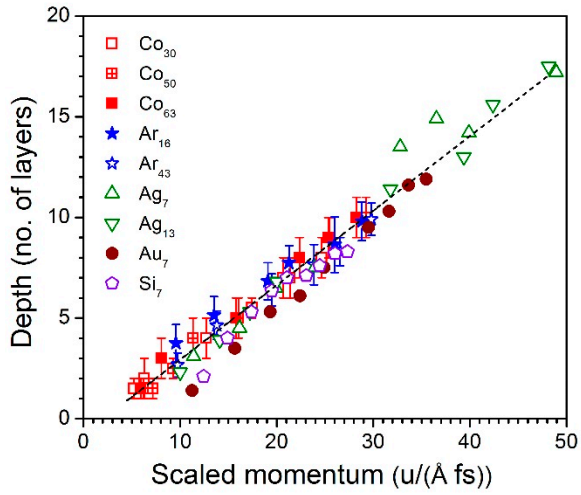

Figure 12. Experimentally-found depth of pits (in number of graphene layers) as a function of scaled momentum (momentum per unite of cross-sectional area of cluster-surface interaction) for different cluster species and sizes. The dashed line represents the best linear fit. The dependence is based on the data published in [108,111,133,159].

3. Functional Nanoparticle-Based Materials

Interest to the practical use of NPs, nanoparticulate films and composites containing NPs comes from different fields. Small particles have a high ratio of surface-to-volume atoms, thus, becoming ideal objects to exploit properties of the outer atoms/surface sites, which play a key role in catalytic applications [161,162]. An ability to control the particle size and composition brings new routes for tuning magnetic properties and creating novel magnetic media [33,163,164]. The phenomenon of localised surface plasmon resonance (LSPR), giving rise to characteristic optical extinction and strong local electromagnetic field enhancement [165], is currently of significant practical interest for applications in sensing, detection and imaging, as well as for optical components and collar cell technologies stimulating the development of novel and sophisticated NP-based systems [166–170]. Controllable assembling of NPs into films or composites allows for conductivity tuning from the variable range hopping to metal-like charge transfer mechanisms opening a way for the fabrication of unique electronic and electro-mechanical devices [171–175]. The NP-filled materials are also of high interest for microwave technologies, bactericidal coatings and membranes, as well as for the formation of surfaces with controlled morphology, wettability and adhesion [176–179].

3.1. Catalytic Applications of Size-Selected Clusters

In sub-nanometre particles, the majority of atoms is located on the surface. These atoms are low-coordinated, thus, promoting a chemical activity. One such example is gold, which is known to be a relatively poor catalyst in bulk but showing considerable catalytic support on the nanoscale in a number of reactions [180,181], for example, oxidation of H_2 and CO, just to mention one of the first publications on this topic [182]. Shrinking the NP size below a hundred atoms also brings into play the quantum phenomena changing the electronic structure and, thus, affecting the chemical properties [183]. Varying the size on the scale of ±1 atom can dramatically change the catalytic efficiency of very small clusters [184,185]. The surrounding medium or supporting substrates are also found to play an important role; metal clusters deposited on oxide surfaces strongly change the catalytic properties due to a charge transfer that, for instance, turns inactive gold and palladium NPs into active catalysts [162,184,186,187]. Tiny Cu_n clusters is another example. In contrast to the gas-phase Cu_n clusters, which are more difficult to oxidize the smaller they are, the supported on amorphous alumina Cu_4 were found to be oxidized easier compared to Cu_{12} and Cu_{20} [188]. This can be seen in the theoretically-obtained phase diagrams presented in Figure 13. The predictions were proven

by experimentally-measured temperature at which the transition from $Cu_nO_{n/2}$ to Cu_n occurs in a H_2-rich environment [188]. The studies of small metal clusters and also of metal alloys have shown that expensive metals can be substituted by cheaper ones while keeping the catalytic efficiency at the same level [161,189]. Since the literature on the catalytic studies of supported metal NPs is numerous, we will overview only the advantages of the cluster beam technique for this field.

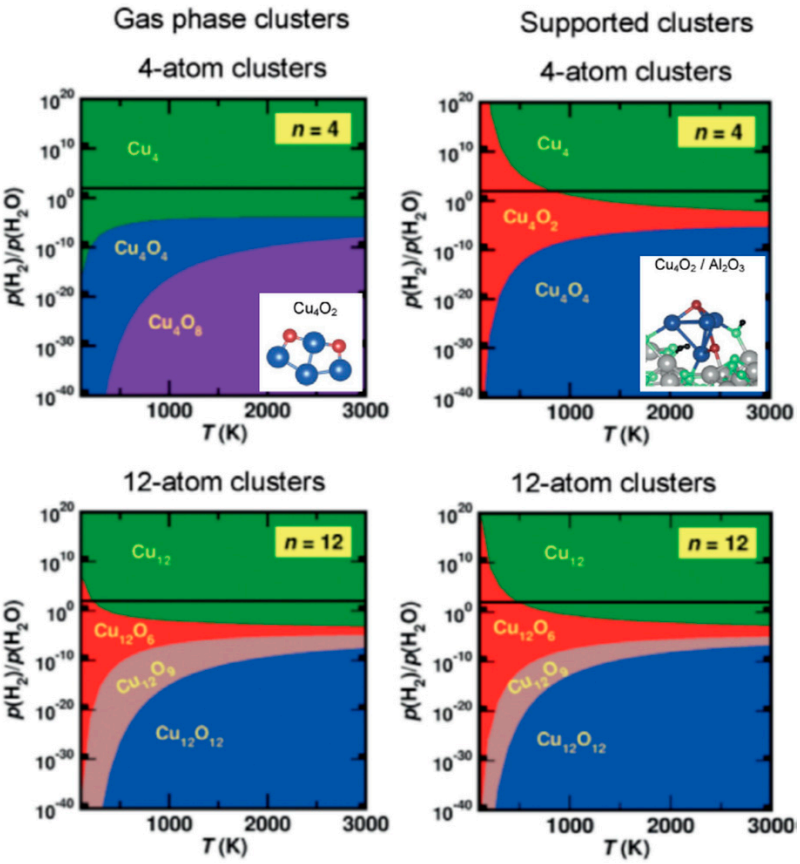

Figure 13. The ratio of the partial pressure of H_2 and H_2O for gas-phase (**left**) and supported on amorphous alumina (**right**) Cu_4 and Cu_{12} clusters as a function of temperature. The green, red and blue areas indicate Cu_n, $Cu_nO_{n/2}$ and Cu_nO_n phases, respectively. Inserts show the calculated lowest energy structures for Cu_4O_2 clusters. Reprinted from [188] with permission from Wiley-VCH.

The main advantages are (i) the size selection to single atom precision for the clusters consisting of up to 2–3 tens of atoms [56,190]; (ii) formation of binary and ternary NPs, as well as core@shell structures [6,44,47,48,191]; and (iii) deposition on any desired substrate with controllable coverage [60]. These pros make the gas aggregation techniques an advantageous tool for the study of model catalysts.

The oxidation activity of tiny Cu_n clusters has been mentioned before. These clusters were also found to be efficient in CO_2 conversion to methanol, $CO_2 + 3H_2 \geq CH_3OH + H_2O$. The turnover rate of about 4×10^{-4} molecules per copper atom and second was reached [192]. Interestingly, the highest rate was found for Cu_4/Al_2O_3 exceeding the activities of other small supported clusters. Strong size-selective reactivity was also observed in CO oxidation on sub-nanometre Ag_n clusters supported on titania [193]. More examples of size-selectivity of various types of model catalyst NPs can be found in [161,189]. It is important to stress that the use of ultra-small NP acting as individual catalytic sites significantly reduces expenses, especially for precious metals. The formation of core@shell structures with cores of less expensive metals and shells composed of active species can also have a considerable economic effect. Generally, core@shell NPs is a class of materials that has recently received increased attention due to a number of advantages for catalysis [194]. In particular, synergetic effects caused by core-shell electron exchange can considerably increase catalytic activity as, for example,

found for Pt-Pd systems [195]. Since multiple-target magnetron sources allow precise control of the core and shell growth in one step [6,47], the gas aggregation approach brings large benefits in the development of new model catalysts. Similar to core@shell structures, alloys can also exhibit a synergistic effect enhancing catalytic activity. For example, Pd_6Ru_6 clusters showed far superior performance in alkene hydrogenation compared to the monometallic analogues of Pd and Ru, as well as other particles like Cu_4Ru_{12}, which were also used to catalyse this reaction [196]. Ag_9Pt_2 and Ag_9Pt_3 bimetallic clusters supported on alumina were observed to be more stable while enabling the same catalytic efficiency of CO oxidation as pure Pt_n [197]. Mass-selected NiFe NPs were found to be perfect model systems providing fundamental insights into the water splitting reaction [198]. Engineering of gas aggregated Ni-Mo-S NPs allowed for tuning their morphology, i.e., the abundances of edge sites, thus, affecting catalytic activity, for example in the removal of sulphur from fossil fuels [199].

Disadvantages of the gas-phase aggregation methods for industrial catalytic applications are the requirement to vacuum and relatively low production rate of clusters sources. A typical cluster beam setup enabling the formation and deposition of sub-nanometer particles would produce below 1 microgram of catalyst per hour [4]. However, the recent development of a new approach for NP gas aggregation, so-called matrix assembly cluster source, brings hope for a breakthrough, as it promises to reach the gram scale in the production of supported size-selected metal NPs [40].

3.2. Magnetic NP-Based Media

The origin of magnetic ordering in the solids is based on the exchange interaction of electrons and spin imbalance. Compared to the solid-state, clusters can represent different symmetry (or broken symmetry) and reduced coordination of surface atoms causing a local increase of moments. For the atomic aggregates of Fe, Co and Ni, known as ferromagnetic materials in bulk, a significant increase of spin moment was found with decreasing the size; also a contribution of the orbital moment can become considerable [200,201]. Free clusters of other transition metals, like Rd_n, Ru_n, Pd_n, Gd_n and Cr_n, were also observed to exhibit enhanced magnetic moments [202,203]. However, analysis of magnetic phenomena of free/isolated clusters is out of the scope of this paper and the reader can be addressed to extensive reviews, for example [204,205].

Clusters of 3d ferromagnetic metals were also found possessing enhanced magnetic moments while being supported on a substrate or embedded into a matrix [164,205,206]. Larger moments were observed on weakly-coupled surfaces like insulators, sp-metals or metals with filled d-band, i.e., some type of hybridization between the cluster and host atoms took place. This phenomenon is found to be important for alloy and core@shell clusters representing systems of 3d metals with other transition metals like Pt, Pd, Au, Ag and W [206–208]. Although many found dependences of magnetic properties on cluster size, species and supporting/surrounding matrix still require a more thorough study, the cluster beam method showed excellent capabilities for varying the magnetic properties on the nanoscale. For instance, core@shell particles can be created in the gas aggregation in one step considering the liquid (L) and solid immiscibility of given components A and B (see Figure 14a) and the difference in surface energy (see Figure 14b). Alloying can undergo for small particles, while with the size increase the positive enthalpy of mixing can lead to the phase separation upon condensation (see Figure 14c) and, thus, giving a possibility to control the particle properties including the magnetic ones [208]. Varying the cluster composition/structure or filling factor of NPs in the matrix allows for tuning the coercive force, saturation magnetization and blocking temperature of superparamagnetic/ferromagnetic transition [164,209,210]. The latter is one of the main suppressions for use of small NPs in high-density memory devices; with decreasing size, one becomes confronted by the superparamagnetic limit. A possible solution could be the use of antiferromagnetic surrounding to enhance the anisotropy of a ferromagnetic NP [211]. Apart from the use of clusters in the formation of materials exhibiting giant magnetoresistance, the gas aggregation method provides excellent capabilities to produce granular films with enhanced tunnelling magnetoresistance [212].

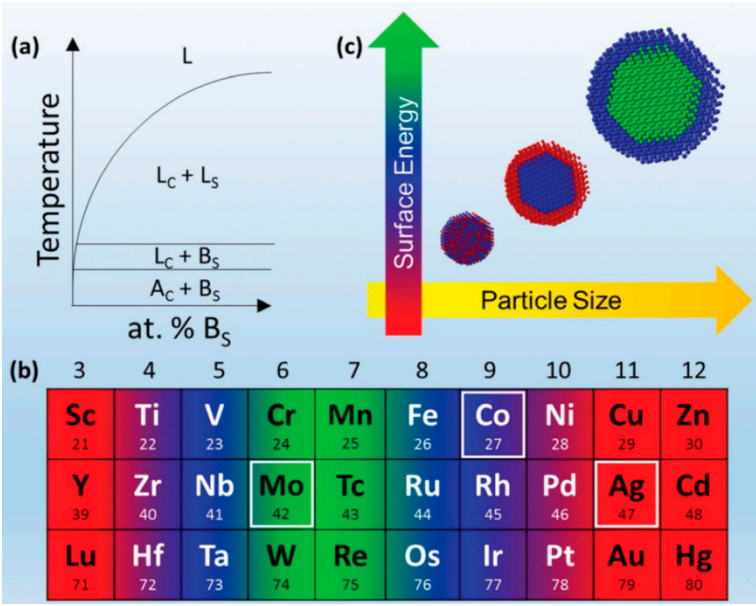

Figure 14. (**a**) Schematic phase diagram of a system with liquid immiscibility, where A_C and B_S are the core and shell materials, respectively. (**b**) The relative surface energies for groups 3–12 of the periodic table (green > blue > red). (**c**) Design concept summary: larger particles with different surface energies will form core-shell structures and blue elements (from groups 4, 5, 8, 9) can be placed in either the core or the shell. Reprinted from [208] with permission from Wiley-VCH.

When forming layers of supported NPs or composites with embedded ones, the surface/volume fraction plays an important role. For an individual cluster of ferromagnetic material, a uniaxial anisotropy with a random orientation of an easy magnetization axis is typical. Decreasing the distance between the NPs to a few lattice constants causes an overlap of the surface electronic wave functions and exchange coupling. Further increase of cluster surface coverage or volume fraction leads to the enhancement of the susceptibility and increase of coercivity [213] until percolation. Beyond the percolation threshold, a correlated super-spin state can be reached. This situation can be described using the parameter characterizing the relative strength of the anisotropy H_r and exchange H_{ex} magnetic fields, $\lambda_r = H_r/H_{ex}$ [163]. For $\lambda_r > 1$, the contribution of the exchange field is small and magnetic vectors of individual particles have random orientation following intra-particle anisotropy axes. With decreasing intra-particle anisotropy, the magnetization of neighbouring particles becomes nearly aligned forming a correlated super-spin but the deviations from perfect alignment can cause a smooth rotation of the magnetization within the magnetic correlation length proportional to $1/\lambda_r^2$. Such superparamagnetic layers show a significant increase of susceptibility and very low coercive filed at room temperature compared to isolated Fe or Co clusters.

NPs with superparamagnetic properties are of wide interest in biological applications: drug delivery, bio-sensing and bio-separation [214]. However, NPs (Fe, Co or allows with other metals) produced by chemical means or physical methods others than gas-phase aggregation are typically efficient enough while being cheaper and simpler. Hence, to our best knowledge, the cluster beam technique is not much in use in this field.

3.3. NPs for Enhanced Sensing and Detection

Cluster assembled nanostructures, which can be obtained using a combination of standard lithography technique and cluster beam deposition, represent a simple method for the formation of electrical contacts and electronic components on the nanoscale. One of such examples is shown in Figure 6, where a nanowire is produced by Bi_n cluster deposition using a mask. It was found that the percolation threshold ensuring the formation of conductive passes through the assembly can be shifted

to very low surface coverages of NPs [215]. Controlling the coverage allows tuning the resistance of the assembled metal nanostructures [174]. This capability was used for the fabrication of passive electronic components (resistors and capacitors) by patterned cluster deposition on paper [61]. An example of resistor arrays formed by gold NPs on plain paper is shown in Figure 15. An advantage of the cluster beam technique is in a wide choice of species (both metals and semiconductors) for NP formation.

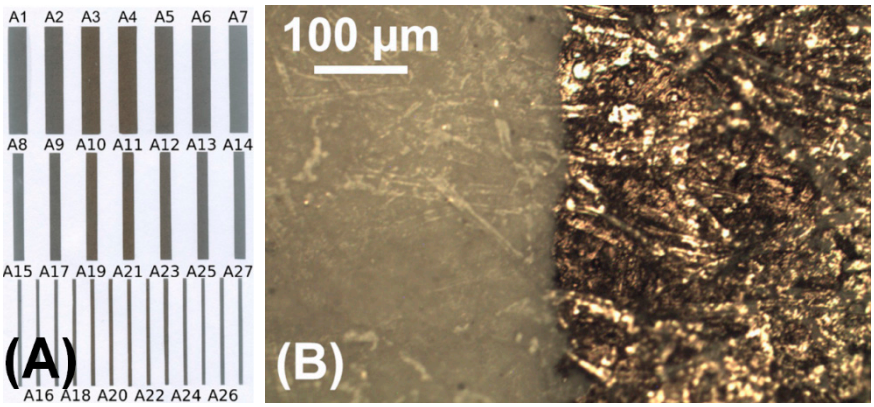

Figure 15. (**A**) Photograph of a set of resistors printed in a one-step process with gold NPs on plain paper. Height of stripes (resistors) is 30 mm, width varies from 1 (bottom) to 5 (top) mm. (**B**) Optical microscopy image of an individual resistor border. Reprinted from [61] with permission from AIP publishing.

Deposited NP assemblies or films were also found to be sensitive to the environmental conditions, i.e., changing the conductance under exposure to some gases. One of the examples are tin oxide nanoclusters (between 3–10 nm in diameter) prepared as a few monolayer thick films which were shown to be highly and fast responsive to hydrogen and ammonia at relatively low temperatures (80–200 °C) by a considerable change of the resistance [216]. Hydrogen sensors based on percolation and tunnelling conductance were also fabricated using Pd_n clusters [217]. In [218], a systematic approach for fabrication of sensor batches on the microscale utilizing hotplates was suggested: NPs of different metal oxides, such as SnO_2, TiO_2, WO_3, Fe_2O_3 etc. could serve for gas sensing.

Cr NPs deposited between silver electrodes fabricated on the polyethylene terephthalate (PET) film were shown to be efficient as strain sensors [175]. A compressive or tensile strain applied to such film changes the inter-particle distance modifying the percolation paths and, thus, the resistance. The sensors have shown much higher gauge factors compared to typical metal foil-based analogues especially for high values of applied strain where the foil-based gauges fail due to cracking. Recently, such approach based on deposited gas aggregated Pd NPs has been suggested for the formation of pressure sensors (see Figure 16) with a resolution as high as 0.5 Pa [219].

Another very widely used method of enhanced sensing is based on the utilisation of LSPR in metal (mostly coinage, Au, Ag and Cu) NPs [165,220]. The cluster beam technique is a very efficient tool allowing the formation of very pure particles with enhanced chemical stability, controlled size and surface coverage, thus, bringing great capabilities for plasmonic property tuning. It has been shown that change of inter-particle distance with increasing surface coverage leads to stronger near-field coupling among metal NPs, thus, allowing for precise control of the plasmon band spectral position. A nearly linear dependence of the band maximum wavelength on the deposition time between ca. 390–570 nm has been demonstrated for the soft-landed gas aggregated Ag NPs [221]. High purity and perfectness of the NP crystalline structure were found to be key factors for strong chemical resistance leading to long-time stability of the plasmonic properties in ambient conditions, which is a very important property for the utilisation of NP-based matrices in surface-enhanced Raman spectroscopy (SERS). Such long-term stability was demonstrated for the gas-aggregated silver [222] and copper [223] NPs (see Figure 17). For the latter, the LSPR stability was additionally promoted by an UV-ozone treatment, which led to the rapid growth of an oxide shell protecting the NP against gradual atmospheric oxidation.

The use of Al NPs is important for some applications where the LSPR resonance is required in UV spectral interval. However, Al is prone to oxidation in ambient air. Therefore, NPs must be embedded in a matrix. Such a strategy was realised in [224], where Al clusters were embedded into 50 nm thick C:H matrix prepared under the simultaneous deposition of the plasma polymer. The composite films demonstrated well-pronounced plasmon bands with maxima between 255–307 nm depending on the particle size. Metal cluster deposition into polymers also opens a way for the production of composite films with the stable tuning of the optical extinction under cyclic compression/stretching [169,225]. One more area of plasmonic properties utilization can be an enhancement of solar cell efficiency. It was recently demonstrated that the deposition of gas-aggregated Ag NPs considerably increases the optical absorption of amorphous Si layers [170].

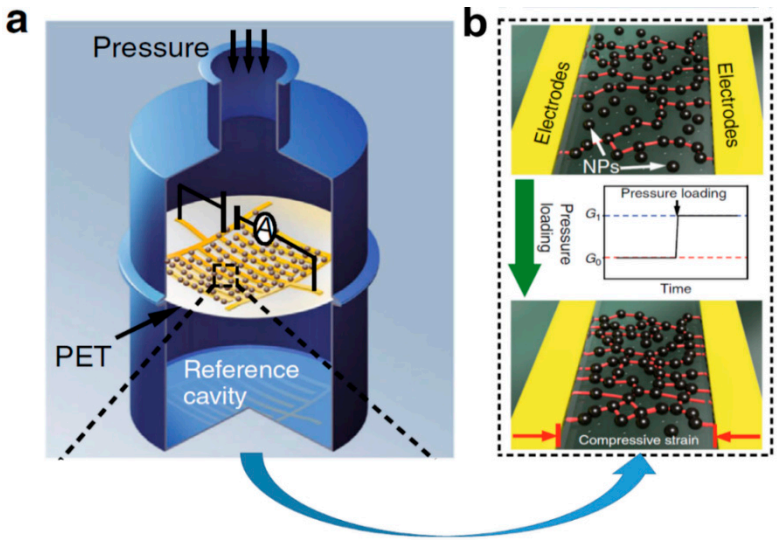

Figure 16. Schematic pictures of a pressure sensor: (**a**) piezoelectric barometric sensor prototype in cross-section and (**b**) operating principle. Red lines linking NPs represent percolation pathways that may exist in arrays. When pressure is loaded, more pathways are generated so that the lines become denser and the resistance decreases. Reprinted from open-access source [219].

Another field in which the use of nanoparticles for enhanced biodetection receives increasing attention is laser desorption/ionization mass spectrometry (LDI MS) [226–229]. In a conventional matrix-assisted LDI (MALDI) technique, the analyte to be studied is embedded into an organic matrix that controls the energy transfer between the incident laser beam and matrix/analyte and allows for the protonation of laser desorbed analyte molecules without their substantial fragmentation [230]. Such produced ionized molecules are subsequently detected by time-of-flight mass spectrometer (TOF-MS). Due to the "soft" ionization process and detection capability of TOF-MS it is possible to detect large molecules with masses up to several hundreds of kDa that makes this technique highly valuable in diverse fields including medical diagnostics, biodefense, clinical chemistry, environmental microbiology, food industry, proteomics or forensic science [231–238]. However, the use of an organic matrix in MALDI possesses critical drawbacks: the poor signal reproducibility due to the inhomogeneous distribution of the analyte in a matrix, limited spatial resolution for imaging or complications in small-molecule detection (the self-ionisation of the organic matrix may interfere with the signal originating from the analyte in the low-mass spectral region). Aforementioned limitations of MALDI may be at least partially overcome if the organic matrix is substituted by inorganic with noble metal NPs (e.g., [239–242]). This method, which is termed as nanoparticle assisted laser desorption/ionization mass spectrometry (Nano-PALDI MS), relies on the ability of NPs to effectively enhance both the desorption and ionization of analyte molecules through the laser-induced heating of the NPs [243] and injection of hot LSPR electrons to the analyte molecule [244]. Although different strategies were developed for the incorporation of NPs into/onto an analyte, the cluster beam deposition

technique offers several advantages. Among them, the most important is the possibility to deposit a controlled number of NPs with well-defined properties and high purity onto relatively large areas with good spatial homogeneity. Recently, it has been shown that size of particles matters in Nano-PALDI measurements, thus, emphasising one more advantage of the cluster beam technique [245]. Thus, the features, which are characteristic for the gas aggregation sources, enable to form matrixes for quantitative, reproducible and sensitive detection of small biomolecules [246,247] as well as imaging of lipids in rat kidney [248], heart or brain tissues [249,250].

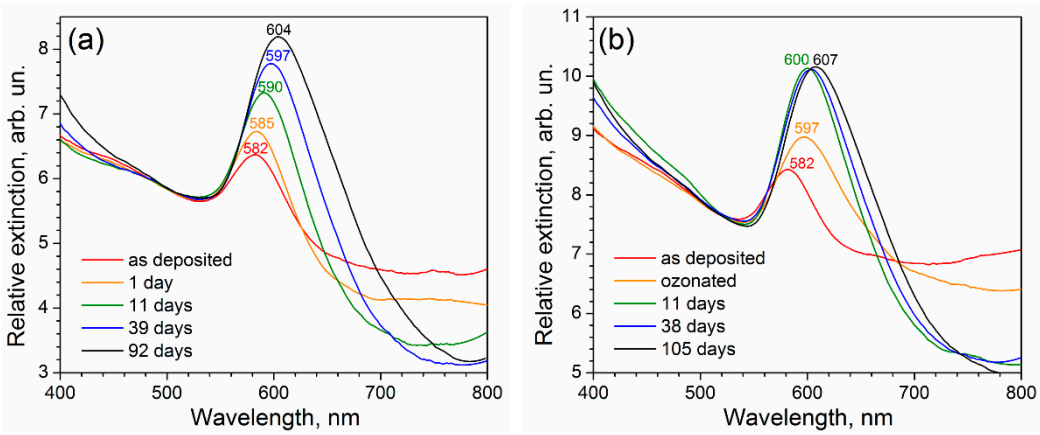

Figure 17. Time evolution of LSPR band for Cu NPs with mean diameter of 19 nm (**a**) kept in ambient air and (**b**) UV-ozone treated for 30 min. and kept in ambient air. Numbers in the panels indicate wavelengths of the band maxima.

3.4. Coatings and Composite Films

Despite the unique properties of NPs and their arrays discussed in the previous sections, one of the limiting factors for their real applications is a weak surface-particle interaction that is a common situation in the case of soft-landing. Due to this, the NP deposits may be easily removed from the surface that hampers their possible use. The high attention is consequently devoted to the development of strategies that enable to fix the NPs on a surface without alteration of their functional properties.

The first approach is based on the implantation of clusters composed of heavy elements into soft materials. As already mentioned in Section 2.3, this may be achieved at kinetic energies of impacting projectiles below the cohesive cluster energy. The typical example represents the embedment of metallic clusters into polymeric substrates by means of supersonic cluster beam implantation (SCBI) developed at the University of Milano [152,251,252]. It has been demonstrated that nanometre size particles may penetrate into a polymeric substrate to the depth of several tens of nanometres while avoiding drastic alteration of the polymer properties typical for NP formation by ion implantation means [253]. Fabricated by SCBI metal/polymer nanocomposites were recently employed as highly deformable elastomeric electrodes with the ability to sustain cyclical stretching [251], mechanical-electro-optical modulators [254], deformable gratings for hyperspectral imaging [255] or stretchable electrodes for the recording of electrical brain activity [252]. Furthermore, such materials are highly promising in the rapidly evolving field of soft robotics [173].

The second method to fix clusters on a substrate utilises their partial or full embedment into a polymeric substrate upon its moderate heating. This approach makes use of the difference in surface energy between metals (in a common situation above 1000 mJ/m^2) [256] and polymers (typically below 100 mJ/m^2) [257]. To minimise the tension at the interface, metal clusters tend to immerse into the polymeric substrate (Figure 18a) until an equilibrium state is reached that is given by [258]:

$$\gamma_{NP} = \gamma_{NP/P} - \gamma_P \cos\varphi \quad (3)$$

where γ_{NP}, $\gamma_{NP/P}$ and γ_P stand for the tension at the interface of NP/air, NP/polymer and polymer/air, while φ is the contact angle as depicted in Figure 18b. In this simplified scenario, that does not account for the forces related to the possible substrate deformation or formation of wetting layer, it is possible to determine the height h of nanoparticle with a radius r above the substrate by [258]:

$$h = r(1 + \cos\varphi). \tag{4}$$

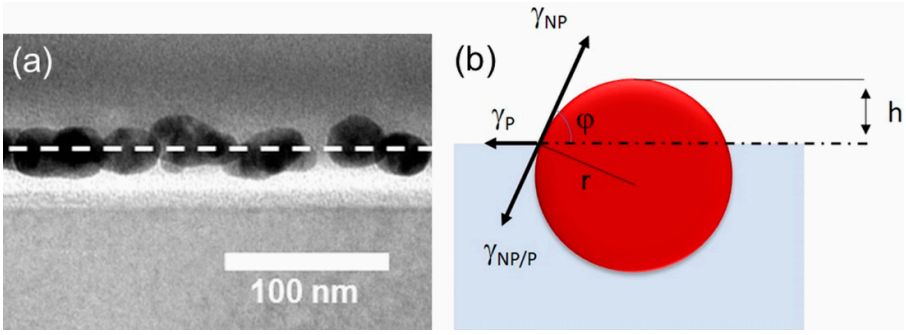

Figure 18. (**a**) High resolution TEM image of Ag NPs partially embedded into PMMA layer with surface indicated by dashed line (reprinted from open-access source [259]) and (**b**) schematic image of NP embedding into soft material (see text for details).

The ability of NP to embed into a soft polymer is substantially promoted when the polymer is heated at a temperature close to its glass transition point at which the flexibility and mobility of polymeric chains increase facilitating, thus, the cluster immersion.

This technique was recently used for the partial embedment of copper, silver and Ti/TiO_x NPs into spin-casted PMMA and polystyrene films [43,258–261]. Such prepared materials may be used either as stable plasmonic-based transducers for protein sensing [259] or as antibacterial coatings [43]. Furthermore, the combination of heat-induced embedding with surface patterning by electron beam lithography represents an interesting option for the facile production of 2D nanoparticle patterns with the desired configuration. In this case, a procedure based on the fabrication of patterned PMMA/polymethylglutarimide (PMGI) coatings, followed by cluster deposition, annealing step and PMMA lift-off (Figure 19) may be employed [261]. An example of such fabricated linear arrays of size-selected Cu NPs is presented in Figure 19 in the dashed circle.

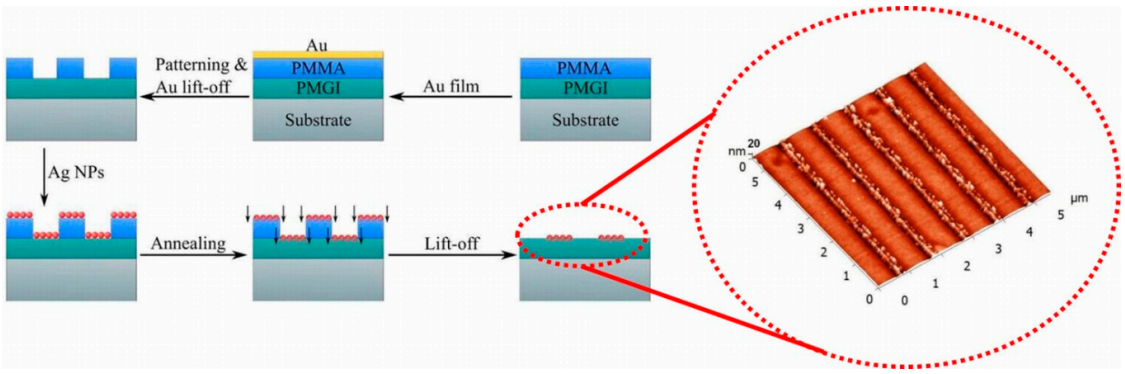

Figure 19. Schematic illustration of the procedure for formation of ordered NP arrays (see text for details) and AFM image of 200 nm wide strips of Ag NPs fabricated by this method. Reprinted from [261] with permission from Cambridge University Press.

NPs may be fixed on a surface also by a thin layer that is deposited over the NP array. Although the overcoat film may be produced by various techniques, the most frequently used are plasma-based deposition techniques (magnetron sputtering, plasma-enhanced chemical vapour deposition, and vacuum

evaporation) that are fully compatible with the vacuum nature of cluster beam method and, thus, the deposition of both NP arrays and fixation layer may be performed in a single apparatus. This is a rather important feature as it avoids exposure of NP deposits to ambient atmosphere and, hence, limits possible contamination or modification of reactive particles when in contact with air. Furthermore, the proper selection of the overcoat material may not only provide the desired fixation of NPs but also add a new functional property to the resulting coatings. The representative example of this is the fabrication of antibacterial coatings based on Ag or Cu NPs. In this case, the fixation layer acts also as a barrier that controls the release of bactericidal ions from the coatings into the liquid environment and with it connected antibacterial efficiency of such nanomaterials [262–265].

In addition, the 3D character of NPs provides a roughness to such prepared coatings. The possibility, on the one hand, to independently tune the surface chemical composition that is given solely by the properties of the overcoat material and, on the other hand, the surface roughness that is primarily given by the size and number of NPs in the base layer, paves the way for the production of nanostructured materials with well-defined interfacial properties. This enabled production of surfaces with tailor-made wettability that may range from super-hydrophilic to super-hydrophobic (e.g., [60,266–273]), superwettable textiles for versatile oil/water separation with antibacterial properties [274] or nanostructured titanium coatings that mimic the surface roughness of a bone and, thus, facilitate the growth of osteoblasts [275]. Obviously, the sequence of deposition of NP and their subsequent overcoating may be repeated that allows for the fabrication of multiple stacks of particle and matrix layers [276]. For instance, in the recent study [277] multi-stack coatings composed of AgPt or AgAu NPs embedded in SiO_2 matrix were fabricated exhibiting reproducible diffusive memristive switching (see Figure 20).

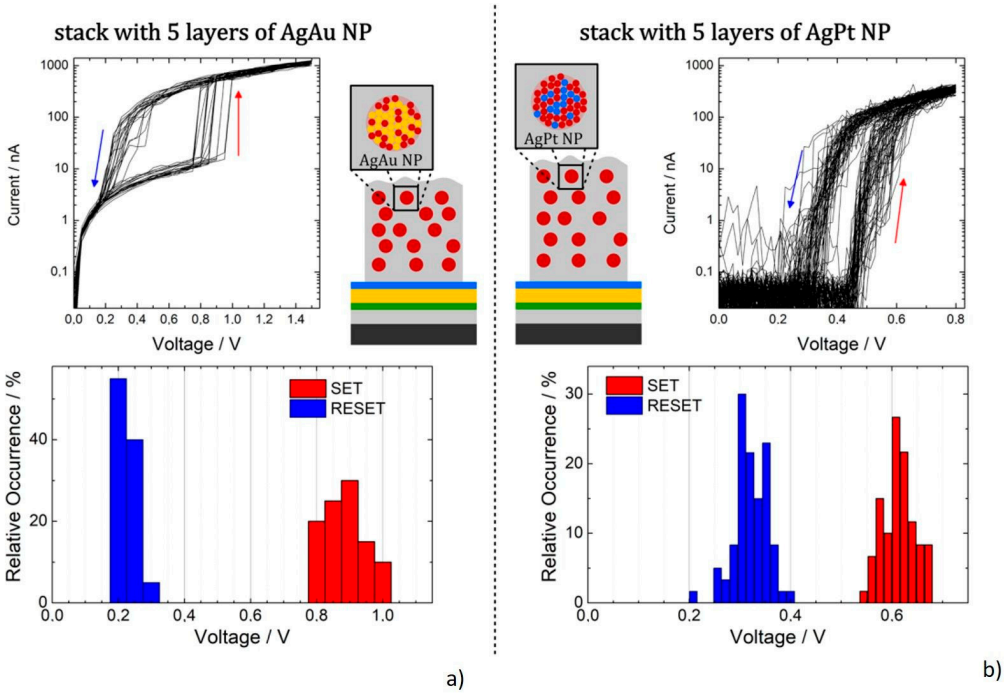

Figure 20. Multi-stack nanoparticle-based memristive devices relying on (**a**) AgAu and (**b**) AgPt nanoparticles exhibit diffusive memristive switching characteristics. For AgAu NP device, the switching characteristics are depicted for 20 consecutive cycles (top) with 2 nm SiO_2 separation layers. The corresponding histogram (bottom) shows a narrow distribution of SET (around 0.89 V) and RESET (around 0.23 V) voltages with a clear separation in between. For AgPt nanoparticle-based multi-stack device with SiO_2 separation layers of 4 nm each, the switching characteristics are depicted for 60 consecutive cycles (top) and the corresponding histogram (bottom) shows a narrow distribution of SET (around 0.61 V) and RESET (around 0.32 V) voltages with a clear separation in between. Reprinted from open-access source [277].

Finally, both the cluster beam and matrix deposition may be performed simultaneously [224,278,279]. This approach was among others successfully tested for the synthesis of Ag/a-C:H and Cu/a-C:H coatings using the deposition system schematically depicted in Figure 21a [280,281]. It consists of a magnetron-based gas aggregation source of metal NPs and a radio-frequency (RF) excitation electrode employed for the plasma polymerisation of n-hexane. The substrate to be coated was placed directly on the RF electrode and was positioned perpendicular to the beam of incoming NPs. This configuration enabled the production of metal/a-C:H nanocomposites (Figure 21b) with a variable number of embedded NPs that was controlled by the magnetron current and mechanical properties of a-C:H matrix regulated by the applied RF power. In a subsequent study [282] it was shown that under optimized conditions the produced Ag/a-C:H coatings deposited on Ti substrates provide excellent antibacterial performance against both Gram-negative (*Escherichia coli*) and Gram-positive (*Staphylococcus aureus*) bacteria and good biocompatibility, i.e., features needed in orthopaedics and other biomedical implants.

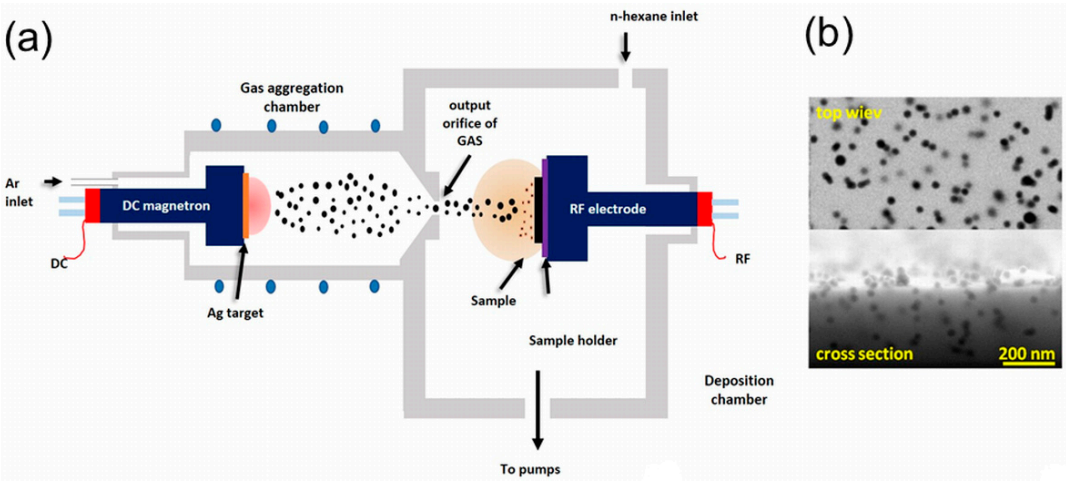

Figure 21. (**a**) Schematic representation of the experimental setup employed for the production of metal/a-C:H nanocomposites and (**b**) SEM images of the top view and cross-section of fabricated Ag/a-C:H coatings. Reprinted from [281] with permission from John Wiley and Sons.

4. Summary and Outlook

The main goal of this review was to overview and analyse the current state of the knowledge regarding the synthesis of nanomaterials using gas aggregation sources and outline their possible applications. As has been shown, the cluster beam deposition/implantation represents a very versatile way of preparing NP-assembled systems and coatings whose structure and functional properties can be tuned by beam parameters and deposition/implantation conditions (e.g., kinetic energy of NPs, their size, composition and structure, as well as properties of substrates or co-deposited material). Based on intensive experimental and theoretical studies of interactions of gas-aggregated NPs with various solid-state substrates, the basic mechanisms leading to the resulting structure of NP arrays/films and NP containing composites have been described and understood in the past two to three decades. This detailed knowledge subsequently paved the way for the rational and effective synthesis of novel NP-based materials with tailor-made structures that are applicable in numerous fields covering novel catalytic systems, magnetic media, platforms for sensing and detection, manufacturing of advanced electrical or electro-mechanical devices, including memristive materials or components for flexible electronics as well as biomedical tools. However, it is also important to note that, despite many advantages the cluster beam method offers, and the enormous development of the gas aggregation technique in past decades, the use of cluster sources at the industrial level is still relatively sparse.

There are several reasons for this paradoxical situation. First, the production capacity of NPs by low-pressure gas aggregation sources reaches only tens of mg per hour at present. This is relatively low,

especially when compared with NP production techniques based on wet chemical methods, ball-milling, laser ablation in liquids [283–285], large-area atmospheric pressure glow discharges or plasma enhanced chemical vapour deposition [286–288] and utilization of the microplasma approach [289]. Therefore, the possible scale-up of the deposition systems and testing of new concepts of gas aggregation sources are nowadays under study intending to meet the requirements of industry on the quantity of synthesized NPs, areas that may be coated or the possibility to perform roll-to-roll deposition at sufficiently high speeds. The second important issue is related to the effectiveness of the NP production in terms of better utilisation of the source material, thus, reducing the costs and prolonging operation time of the cluster sources. In this filed, new technological solutions are urgently needed. Another aspect that may promote the wider utilisation of gas-phase synthesis of NPs is to make full use of the potential of this technique for the production of multi-component systems. This refers not only to the production of functional nanocomposites, in which the NPs are embedded in a hosting matrix, but also to the fabrication of multi-component NPs per se. Related to the latter, new highly promising strategies have been recently proposed and tested by different research groups. They utilize (i) a multi-magnetron approach, in which two or more sources of different materials are placed into one aggregation chamber; (ii) alloy or segmental multi-component sputtering targets; (iii) a combination of simultaneously running magnetron sputtering and plasma polymerization; or (iv) systems that are based on the in-flight coating/modification of NPs before their landing onto the substrate. However, the control of the structure and composition of multi-component NPs is still very challenging as the growth process is much more complex compared to mono-material particles. Due to this, the unavoidable prerequisite for the further development in this direction is the deeper understanding of the processes taking part during the growth and transport of NPs in the aggregation chamber or interaction of NPs with an auxiliary plasma used for their in-flight modification. This requires targeted experiments and novel numerical simulations whose complexity is at the edge of the computational capacity of current computers. Finally, novel classes of nanomaterials—nanofluids—with unique properties are nowadays discussed in the community [290,291]. In this case, the gas aggregation sources are believed to represent a powerful and effective means of production of such materials as the cluster beam deposition is, in principle, compatible with any liquid with low vapour pressure. This may open the way for the direct deposition of NPs into such liquids.

Author Contributions: Conceptualization: V.N.P.; writing—original draft preparation: V.N.P. and O.K.; writing—review and editing: V.N.P. and O.K.; visualization: V.N.P. and O.K. All authors have read and agreed to the published version of the manuscript.

Funding: This research received no external funding.

Conflicts of Interest: The authors declare no conflict of interest.

References

1. Barhoum, A.; Makhlouf, A.S.H. (Eds.) *Emerging Applications of Nanoparticles and Architecture Nanostructures*; Elsevier: Amsterdam, The Netherlands, 2018. [CrossRef]
2. Milani, P.; Sowwan, M. (Eds.) *Cluster Beam Deposition of Functional Nanomaterials and Devices*; Elsevier: Amsterdam, The Netherlands, 2020. [CrossRef]
3. Deepak, F.L. (Ed.) *Metal Nanoparticles and Clusters: Advances in Synthesis, Properties and Applications*; Springer: Cham, Switzerland, 2017. [CrossRef]
4. Ellis, P.R.; Brown, C.M.; Bishop, P.T.; Yin, J.; Cooke, K.; Terry, W.D.; Liu, J.; Yin, F.; Palmer, R.E. The cluster beam route to model catalysts and beyond. *Faraday Discuss.* **2016**, *188*, 39–56. [CrossRef] [PubMed]
5. Borghi, F.; Podestà, A.; Piazzoni, C.; Milani, P. Growth mechanism of cluster-assembled surfaces: From submonolayer to thin-film regime. *Phys. Rev. Appl.* **2018**, *9*, 044016. [CrossRef]
6. Grammatikopoulos, P.; Steinhauer, S.; Vernieres, J.; Singh, V.; Sowwan, M. Nanoparticle design by gas-phase synthesis. *Adv. Phys. X* **2016**, *1*, 81–100. [CrossRef]
7. Huttel, Y.; Martínez, L.; Mayoral, A.; Fernández, I. Gas-phase synthesis of nanoparticles: Present status and perspectives. *MRS Commun.* **2018**, *8*, 947–954. [CrossRef] [PubMed]

8. Haberland, H. Experimental methods. In *Clusters of Atoms and Molecules*; Haberland, H., Ed.; Springer: Berlin, Germany, 1994; pp. 207–252.
9. Pfund, A.H. Bismuth black and its applications. *Rev. Sci. Instrum.* **1930**, *1*, 397. [CrossRef]
10. Becker, E.W.; Bier, K.; Henkes, W. Strahlen aus kondensierten Atomen und Molekeln im Hochvakuum. *Eur. Phys. J. A* **1956**, *146*, 333–338. [CrossRef]
11. Henkes, W. Notizen: Ionisierung und Beschleunigung kondensierter Molekularstrahlen. *Z. Nat. A* **1961**, *16*, 842. [CrossRef]
12. Henkes, W. Massenspektrometrische Untersuchung von Strahlen aus kondensiertem Wasserstoff. *Z. Nat. A* **1962**, *17*, 786–789. [CrossRef]
13. Dole, M. Molecular beams of macroions. *J. Chem. Phys.* **1968**, *49*, 2240. [CrossRef]
14. Clampitt, R. Abstract: Intense field-emission ion source of liquid metals. *J. Vac. Sci. Technol.* **1975**, *12*, 1208. [CrossRef]
15. Helm, H. Field emission ion source of molecular cesium ions. *Rev. Sci. Instrum.* **1983**, *54*, 837. [CrossRef]
16. Dixon, A.; Ohana, R.; Sudraud, P.; Colliex, C.; Van De Walle, J. Field-ion emission from liquid tin. *Phys. Rev. Lett.* **1981**, *46*, 865–868. [CrossRef]
17. Hagena, O.F. Cluster formation in expanding supersonic jets: Effect of pressure, temperature, nozzle size, and test gas. *J. Chem. Phys.* **1972**, *56*, 1793. [CrossRef]
18. Hogg, E.O.; Silbernagel, B.G. Particle growth in flowing inert gases. *J. Appl. Phys.* **1974**, *45*, 593. [CrossRef]
19. Takagi, T.; Yamada, I.; Sasaki, A. An evaluation of metal and semiconductor films formed by ionized-cluster beam deposition. *Thin Solid Films* **1976**, *39*, 207–217. [CrossRef]
20. Bondybey, V.E. Laser induced fluorescence of metal clusters produced by laser vaporization: Gas phase spectrum of Pb2. *J. Chem. Phys.* **1981**, *74*, 6978. [CrossRef]
21. Dietz, T.G.; Duncan, M.A.; Powers, D.E.; Smalley, R.E. Laser production of supersonic metal cluster beams. *J. Chem. Phys.* **1981**, *74*, 6511–6512. [CrossRef]
22. Kroto, H.W.; Heath, J.R.; O'Brien, S.C.; Curl, R.F.; Smalley, R.E. C60: Buckminsterfullerene. *Nature* **1985**, *318*, 162–163. [CrossRef]
23. Begemann, W.; Meiwes-Broer, K.-H.; Lutz, H.O. Unimolecular decomposition of Sputtered Aln+, Cun+, and Sin+ clusters. *Phys. Rev. Lett.* **1986**, *56*, 2248–2251. [CrossRef]
24. Ganteför, G.; Siekmann, H.; Lutz, H.; Meiwes-Broer, K.-H. Pure metal and metal-doped rare-gas clusters grown in a pulsed ARC cluster ion source. *Chem. Phys. Lett.* **1990**, *165*, 293–296. [CrossRef]
25. Barborini, E.; Piseri, P.; Milani, P. A pulsed microplasma source of high intensity supersonic carbon cluster beams. *J. Phys. D Appl. Phys.* **1999**, *32*, L105–L109. [CrossRef]
26. Greene, J. Review article: Tracing the recorded history of thin-film sputter deposition: From the 1800s to 2017. *J. Vac. Sci. Technol. A* **2017**, *35*, 05C204. [CrossRef]
27. Haberland, H.; Karrais, M.; Mall, M. A new type of cluster and cluster ion source. *Eur. Phys. J. D* **1991**, *20*, 413–415. [CrossRef]
28. Polonskyi, O.; Ahadi, A.M.; Peter, T.; Fujioka, K.; Abraham, J.W.; Vasiliauskaite, E.; Hinz, A.; Strunskus, T.; Wolf, S.; Bonitz, M.; et al. Plasma based formation and deposition of metal and metal oxide nanoparticles using a gas aggregation source. *Eur. Phys. J. D* **2018**, *72*, 93. [CrossRef]
29. Shelemin, A.; Pleskunov, P.; Kousal, J.; Drewes, J.; Hanuš, J.; Ali-Ogly, S.; Nikitin, D.; Solar, P.; Kratochvíl, J.; Vaidulych, M.; et al. Nucleation and growth of magnetron-sputtered Ag nanoparticles as witnessed by time-resolved small angle X-ray scattering. *Part. Part. Syst. Charact.* **2019**, *37*, 1900436. [CrossRef]
30. Hagena, O.F. Cluster ion sources (invited). *Rev. Sci. Instrum.* **1992**, *63*, 2374–2379. [CrossRef]
31. Melinon, P.; Paillard, V.; Dupuis, V.; Perez, A.; Jensén, P.; Hoareau, A.; Pérez, J.; Tuaillon, J.; Broyer, M.; Vialle, J.; et al. From free clusters to cluster-assembled materials. *Int. J. Mod. Phys. B* **1995**, *9*, 339–397. [CrossRef]
32. Milani, P.; Iannotta, S. *Cluster Beam Synthesis of Nanostructured Materials*; Springer: Berlin, Germany, 1999.
33. Binns, C. Nanoclusters deposited on surfaces. *Surf. Sci. Rep.* **2001**, *44*, 1–49. [CrossRef]
34. Binns, C.; Trohidou, K.N.; Bansmann, J.; Baker, S.H.; A Blackman, J.; Bucher, J.-P.; Kechrakos, D.; Kleibert, A.; Louch, S.; Meiwes-Broer, K.-H.; et al. The behaviour of nanostructured magnetic materials produced by depositing gas-phase nanoparticles. *J. Phys. D Appl. Phys.* **2005**, *38*, R357–R379. [CrossRef]
35. Wegner, K.; Piseri, P.; Tafreshi, H.V.; Milani, P. Cluster beam deposition: A tool for nanoscale science and technology. *J. Phys. D Appl. Phys.* **2006**, *39*, R439–R459. [CrossRef]

36. Popok, V.N.; Campbell, E.E.B. Beams of atomic clusters: Effects on impact with solids. *Rev. Adv. Mater. Sci.* **2006**, *11*, 19–45.
37. Popok, V.N. Energetic cluster ion beams: Modification of surfaces and shallow layers. *Mater. Sci. Eng. R Rep.* **2011**, *72*, 137–157. [CrossRef]
38. Yamada, I. Historical milestones and future prospects of cluster ion beam technology. *Appl. Surf. Sci.* **2014**, *310*, 77–88. [CrossRef]
39. Palmer, R.E.; Cao, L.; Yin, F. Note: Proof of principle of a new type of cluster beam source with potential for scale-up. *Rev. Sci. Instrum.* **2016**, *87*, 46103. [CrossRef] [PubMed]
40. Cai, R.; Cao, L.; Griffin, R.; Chansai, S.; Hardacre, C.; Palmer, R.E. Scale-up of cluster beam deposition to the gram scale with the matrix assembly cluster source for heterogeneous catalysis (propylene combustion). *AIP Adv.* **2020**, *10*, 025314. [CrossRef]
41. Shelemin, A.; Kylián, O.; Hanuš, J.; Choukourov, A.; Melnichuk, I.; Serov, A.; Slavinska, D.; Biederman, H. Preparation of metal oxide nanoparticles by gas aggregation cluster source. *Vacuum* **2015**, *120*, 162–169. [CrossRef]
42. Martínez, L.; Lauwaet, K.; Santoro, G.; Sobrado, J.M.; Peláez, R.J.; Herrero, V.J.; Tanarro, I.; Ellis, G.; Cernicharo, J.; Joblin, C.; et al. Precisely controlled fabrication, manipulation and In-Situ analysis of Cu based nanoparticles. *Sci. Rep.* **2018**, *8*, 7250. [CrossRef]
43. Popok, V.N.; Jeppesen, C.M.; Fojan, P.; Kuzminova, A.; Hanuš, J.; Kylián, O. Comparative study of antibacterial properties of polystyrene films with TiO x and Cu nanoparticles fabricated using cluster beam technique. *Beilstein J. Nanotechnol.* **2018**, *9*, 861–869. [CrossRef]
44. Vahl, A.; Strobel, J.; Reichstein, W.; Polonskyi, O.; Strunskus, T.; Kienle, L.; Faupel, F. Single target sputter deposition of alloy nanoparticles with adjustable composition via a gas aggregation cluster source. *Nanotechnology* **2017**, *28*, 175703. [CrossRef]
45. Ayesh, A.I. Size-selected fabrication of alloy nanoclusters by plasma-gas condensation. *J. Alloys Compd.* **2018**, *745*, 299–305. [CrossRef]
46. Xu, Y.-H.; Wang, J.-P. Direct gas-phase synthesis of heterostructured nanoparticles through phase separation and surface segregation. *Adv. Mater.* **2008**, *20*, 994–999. [CrossRef]
47. Martínez, L.; Mayoral, A.; Espiñeira, M.; Roman, E.; Palomares, F.J.; Huttel, Y. Core@shell, Au@TiOx nanoparticles by gas phase synthesis. *Nanoscale* **2017**, *9*, 6463–6470. [CrossRef] [PubMed]
48. Llamosa, D.; Ruano, M.; Martinez, L.; Mayoral, A.; Roman, E.; Garcia-Hernandez, M.; Huttel, Y. The ultimate step towards a tailored engineering of core@shell and core@shell@shell nanoparticles. *Nanoscale* **2014**, *6*, 13483–13486. [CrossRef] [PubMed]
49. Hanuš, J.; Vaidulych, M.; Kylián, O.; Choukourov, A.; Kousal, J.; Khalakhan, I.; Cieslar, M.; Solar, P.; Biederman, H. Fabrication of Ni@Ti core–shell nanoparticles by modified gas aggregation source. *J. Phys. D Appl. Phys.* **2017**, *50*, 475307. [CrossRef]
50. Yin, F.; Wang, Z.-W.; Palmer, R.E. Controlled formation of mass-selected Cu–Au core–shell cluster beams. *J. Am. Chem. Soc.* **2011**, *133*, 10325–10327. [CrossRef]
51. Singh, V.; Cassidy, C.; Grammatikopoulos, P.; Djurabekova, F.; Nordlund, K.; Sowwan, M. Heterogeneous gas-phase synthesis and molecular dynamics modeling of janus and core–satellite Si–Ag nanoparticles. *J. Phys. Chem. C* **2014**, *118*, 13869–13875. [CrossRef]
52. Solar, P.; Hanuš, J.; Cieslar, M.; Košutová, T.; Škorvánková, K.; Kylián, O.; Kúš, P.; Biederman, H. Composite Ni@Ti nanoparticles produced in arrow-shaped gas aggregation source. *J. Phys. D Appl. Phys.* **2020**, *53*, 195303. [CrossRef]
53. Solar, P.; Polonskyi, O.; Olbricht, A.; Hinz, A.; Shmielen, A.; Kylián, O.; Choukourov, A.; Faupel, F.; Biederman, H. Single-step generation of metal-plasma polymer multicore@shell nanoparticles from the gas phase. *Sci. Rep.* **2017**, *7*, 8514. [CrossRef]
54. Kylián, O.; Shelemin, A.; Solar, P.; Pleskunov, P.; Nikitin, D.; Kuzminova, A.; Štefaníková, R.; Kúš, P.; Cieslar, M.; Hanuš, J.; et al. Magnetron sputtering of polymeric targets: From thin films to heterogeneous metal/plasma polymer nanoparticles. *Materials* **2019**, *12*, 2366. [CrossRef]
55. Kylián, O.; Kuzminova, A.; Štefaníková, R.; Hanuš, J.; Solař, P.; Kúš, P.; Cieslar, M.; Choukourov, A.; Biederman, H. Silver/plasma polymer strawberry-like nanoparticles produced by gas-phase synthesis. *Mater. Lett.* **2019**, *253*, 238–241. [CrossRef]

56. Pratontep, S.; Carroll, S.J.; Xirouchaki, C.; Streun, M.; Palmer, R.E. Size-selected cluster beam source based on radio frequency magnetron plasma sputtering and gas condensation. *Rev. Sci. Instrum.* **2005**, *76*, 45103. [CrossRef]
57. Popok, V.N.; Barke, I.; Campbell, E.E.B.; Meiwes-Broer, K.-H. Cluster–surface interaction: From soft landing to implantation. *Surf. Sci. Rep.* **2011**, *66*, 347–377. [CrossRef]
58. Kappes, M.M.; Leutwyler, S. Molecular beams of clusters. In *Atomic and Molecular Beam Methods*; Scoles, G., Ed.; Oxford University Press: New York, NY, USA, 1988; Volume 1, pp. 380–415.
59. De Heer, W.A. The physics of simple metal clusters: Experimental aspects and simple models. *Rev. Mod. Phys.* **1993**, *65*, 611–676. [CrossRef]
60. Petr, M.; Kylián, O.; Hanuš, J.; Kuzminova, A.; Vaidulych, M.; Khalakhan, I.; Choukourov, A.; Slavinska, D.; Biederman, H. Surfaces with roughness gradient and invariant surface chemistry produced by means of gas aggregation source and magnetron sputtering. *Plasma Process. Polym.* **2016**, *13*, 663–671. [CrossRef]
61. Caruso, F.; Bellacicca, A.; Milani, P. High-throughput shadow mask printing of passive electrical components on paper by supersonic cluster beam deposition. *Appl. Phys. Lett.* **2016**, *108*, 163501. [CrossRef]
62. Kratochvil, J.; Stranak, V.; Kousal, J.; Kus, P.; Kylian, O. Theoretical and experimental analysis of defined 2D-graded two-metal nanoparticle-build surfaces. *Appl. Surf. Sci.* **2020**, *511*, 145530. [CrossRef]
63. Meakin, P.; Ramanlal, P.; Sander, L.M.; Ball, R.C. Ballistic deposition on surfaces. *Phys. Rev. A* **1986**, *34*, 5091–5103. [CrossRef]
64. Vold, M.J. Computer simulation of floc formation in a colloidal suspension. *J. Colloid Sci.* **1963**, *18*, 684–695. [CrossRef]
65. Sutherland, D.N. A theoretical model of floc structure. *J. Colloid Interface Sci.* **1967**, *25*, 373–380. [CrossRef]
66. Barabasi, A.-L.; Stanley, H.E. *Fractal Concepts in Surface Growth*; Cambridge University Press: New York, NY, USA, 1995. [CrossRef]
67. Family, F.; Vicsek, T. (Eds.) *Dynamics of Fractal Surfaces*; World Scientific: Singapore, 1991. [CrossRef]
68. Konstandopoulos, A.G. Deposit growth dynamics: Particle sticking and scattering phenomena. *Powder Technol.* **2000**, *109*, 262–277. [CrossRef]
69. Podestà, A.; Borghi, F.; Indrieri, M.; Bovio, S.; Piazzoni, C.; Milani, P. Nanomanufacturing of titania interfaces with controlled structural and functional properties by supersonic cluster beam deposition. *J. Appl. Phys.* **2015**, *118*, 234309. [CrossRef]
70. Bardotti, L.; Jensén, P.; Hoareau, A.; Treilleux, M.; Cabaud, B.; Perez, A.; Aires, F.C.S. Diffusion and aggregation of large antimony and gold clusters deposited on graphite. *Surf. Sci.* **1996**, *367*, 276–292. [CrossRef]
71. Bardotti, L.; Jensen, P.; Hoareau, A.; Treilleux, M.; Cabaud, B. Experimental observation of fast diffusion of large antimony clusters on graphite surfaces. *Phys. Rev. Lett.* **1995**, *74*, 4694–4697. [CrossRef]
72. Deltour, P.; Jensen, P.; Barrat, J.-L. Fast diffusion of a lennard-jones cluster on a crystalline surface. *Phys. Rev. Lett.* **1997**, *78*, 4597–4600. [CrossRef]
73. Ryu, J.H.; Seo, D.; Kim, D.-H.; Lee, H.M. Molecular dynamics simulations of the diffusion and rotation of Pt nanoclusters supported on graphite. *Phys. Chem. Chem. Phys.* **2009**, *11*, 503–507. [CrossRef] [PubMed]
74. Perez, A.; Melinon, P.; Dupuis, V.; Jensen, P.; Prével, B.; Tuaillon, J.; Bardotti, L.; Martet, C.; Treilleux, M.; Broyer, M.; et al. Cluster assembled materials: A novel class of nanostructured solids with original structures and properties. *J. Phys. D Appl. Phys.* **1997**, *30*, 709–721. [CrossRef]
75. Grammatikopoulos, P.; Sowwan, M.; Kioseoglou, J. Computational modeling of nanoparticle coalescence. *Adv. Theory Simul.* **2019**, *2*, 1900013. [CrossRef]
76. Lehtinen, K.E.; Zachariah, M. Energy accumulation in nanoparticle collision and coalescence processes. *J. Aerosol Sci.* **2002**, *33*, 357–368. [CrossRef]
77. Lehtinen, K.E.J.; Zachariah, M.R. Effect of coalescence energy release on the temporal shape evolution of nanoparticles. *Phys. Rev. B* **2001**, *63*, 205402. [CrossRef]
78. Singh, V.; Grammatikopoulos, P.; Cassidy, C.; Benelmekki, M.; Bohra, M.; Hawash, Z.; Baughman, K.W.; Sowwan, M. Assembly of tantalum porous films with graded oxidation profile from size-selected nanoparticles. *J. Nanoparticle Res.* **2014**, *16*, 2373. [CrossRef]
79. Yoon, B.; Akulin, V.; Cahuzac, P.; Carlier, F.; De Frutos, M.; Masson, A.; Mory, C.; Colliex, C.; Bréchignac, C. Morphology control of the supported islands grown from soft-landed clusters. *Surf. Sci.* **1999**, *443*, 76–88. [CrossRef]

80. Carroll, S.J.; Seeger, K.; Palmer, R.E. Trapping of size-selected Ag clusters at surface steps. *Appl. Phys. Lett.* **1998**, *72*, 305–307. [CrossRef]
81. Jensen, P. Growth of nanostructures by cluster deposition: Experiments and simple models. *Rev. Mod. Phys.* **1999**, *71*, 1695–1735. [CrossRef]
82. Jensen, P.; Clément, A.; Lewis, L.J. Diffusion of nanoclusters on non-ideal surfaces. *Phys. E Low-Dimens. Syst. Nanostruct.* **2004**, *21*, 71–76. [CrossRef]
83. Jensen, P.; Clément, A.; Lewis, L.J. Diffusion of nanoclusters. *Comput. Mater. Sci.* **2004**, *30*, 137–142. [CrossRef]
84. Schmidt, M.; Kébaïli, N.; Lando, A.; Benrezzak, S.; Baraton, L.; Cahuzac, P.; Masson, A.; Bréchignac, C. Bent graphite surfaces as guides for cluster diffusion and anisotropic growth. *Phys. Rev. B* **2008**, *77*, 205420. [CrossRef]
85. Pérez, A.; Bardotti, L.; Prével, B.; Jensen, P.; Treilleux, M.; Melinon, P.; Gierak, J.; Faini, G.; Mailly, D. Quantum-dot systems prepared by 2D organization of nanoclusters preformed in the gas phase on functionalized substrates. *New J. Phys.* **2002**, *4*, 76. [CrossRef]
86. Bardotti, L.; Prevel, B.; Jensen, P.; Treilleux, M.; Melinon, P.; Pérez, A.; Gierak, J.; Faini, G.; Mailly, D. Organizing nanoclusters on functionalized surfaces. *Appl. Surf. Sci.* **2002**, *191*, 205–210. [CrossRef]
87. Prevel, B.; Bardotti, L.; Fanget, S.; Hannour, A.; Melinon, P.; Pérez, A.; Gierak, J.; Faini, G.; Bourhis, E.; Mailly, D. Gold nanoparticle arrays on graphite surfaces. *Appl. Surf. Sci.* **2004**, *226*, 173–177. [CrossRef]
88. Melinon, P.; Hannour, A.; Prével, B.; Bardotti, L.; Bernstein, E.; Perez, A.; Gierak, J.; Bourhis, E.; Mailly, D. Functionalizing surfaces with arrays of clusters: Role of the defects. *J. Cryst. Growth* **2005**, *275*, 317–324. [CrossRef]
89. Novikov, S.M.; Popok, V.N.; Fiutowski, J.; Arsenin, A.V.; Volkov, V.S. Plasmonic properties of nanostructured graphene with silver nanoparticles. *J. Phys. Conf. Ser.* **2020**, *1461*, 012119. [CrossRef]
90. Mondal, S.; Chowdhury, D. Controlled deposition of size-selected metal nanoclusters on prepatterned substrate. *Surf. Coat. Technol.* **2020**, *393*, 125776. [CrossRef]
91. Kébaili, N.; Benrezzak, S.; Cahuzac, P.; Masson, A.; Bréchignac, C. Diffusion of silver nanoparticles on carbonaceous materials. Cluster mobility as a probe for surface characterization. *Eur. Phys. J. D* **2009**, *52*, 115–118. [CrossRef]
92. Bardotti, L.; Tournus, F.; Melinon, P.; Pellarin, M.; Broyer, M. Mass-selected clusters deposited on graphite: Spontaneous organization controlled by cluster surface reaction. *Phys. Rev. B* **2011**, *83*, 035425. [CrossRef]
93. Alayan, R.; Arnaud, L.; Broyer, M.; Cottancin, E.; Lermé, J.; Marhaba, S.; Vialle, J.L.; Pellarin, M. Organization of size-selected platinum and indium clusters soft-landed on surfaces. *Phys. Rev. B* **2007**, *76*, 075424. [CrossRef]
94. Tainoff, D.; Bardotti, L.; Tournus, F.; Guiraud, G.; Boisron, O.; Melinon, P. Self-organization of size-selected bare platinum nanoclusters: Toward ultra-dense catalytic systems. *J. Phys. Chem. C* **2008**, *112*, 6842–6849. [CrossRef]
95. Tournus, F.; Bardotti, L.; Dupuis, V. Size-dependent morphology of CoPt cluster films on graphite: A route to self-organization. *J. Appl. Phys.* **2011**, *109*, 114309. [CrossRef]
96. Hou, Q.; Hou, M.; Bardotti, L.; Prével, B.; Melinon, P.; Perez, A. Deposition of AuN clusters on Au(111) surfaces. I. Atomic-scale modeling. *Phys. Rev. B* **2000**, *62*, 2825–2834. [CrossRef]
97. Jimenez-Saez, J.; Pérez-Martin, C.; Jiménez-Rodríguez, J. A molecular dynamics study of atomic rearrangements in Cu clusters softly deposited on an Au(001) surface. *Nucl. Instrum. Methods Phys. Res. B* **2006**, *249*, 816–819. [CrossRef]
98. Järvi, T.T.; Kuronen, A.; Meinander, K.; Nordlund, K.; Albe, K. Contact epitaxy by deposition of Cu, Ag, Au, Pt, and Ni nanoclusters on (100) surfaces: Size limits and mechanisms. *Phys. Rev. B* **2007**, *75*, 115422. [CrossRef]
99. Meinander, K.; Frantz, J.; Nordlund, K.; Keinonen, J. Upper size limit of complete contact epitaxy. *Thin Solid Films* **2003**, *425*, 297–303. [CrossRef]
100. Reichel, R.; Partridge, J.G.; Natali, F.; Matthewson, T.; Brown, S.A.; Lassesson, A.; MacKenzie, D.M.A.; Ayesh, A.I.; Tee, K.C.; Awasthi, A.; et al. From the adhesion of atomic clusters to the fabrication of nanodevices. *Appl. Phys. Lett.* **2006**, *89*, 213105. [CrossRef]
101. Awasthi, A.; Hendy, S.C.; Zoontjens, P.; Brown, S.A.; Natali, F. Molecular dynamics simulations of reflection and adhesion behavior in Lennard-Jones cluster deposition. *Phys. Rev. B* **2007**, *76*, 115437. [CrossRef]

102. Reichel, R.; Partridge, J.G.; Brown, S.A. Characterization of a template process for conducting cluster-assembled wires. *Appl. Phys. A* **2009**, *97*, 315–321. [CrossRef]
103. Carroll, S.J.; Weibel, P.; Von Issendorff, B.; Kuipers, L.; Palmer, R.E. The impact of size-selected Ag clusters on graphite: An STM study. *J. Phys. Condens. Matter* **1996**, *8*, L617–L624. [CrossRef]
104. Di Vece, M.; Palomba, S.; E Palmer, R. Pinning of size-selected gold and nickel nanoclusters on graphite. *Phys. Rev. B* **2005**, *72*, 073407. [CrossRef]
105. Gibilisco, S.; Di Vece, M.; Palomba, S.; Faraci, G.; Palmer, R.E. Pinning of size-selected Pd nanoclusters on graphite. *J. Chem. Phys.* **2006**, *125*, 84704. [CrossRef]
106. Vučković, S.; Svanqvist, M.; Popok, V.N. Laser ablation source for formation and deposition of size-selected metal clusters. *Rev. Sci. Instrum.* **2008**, *79*, 73303. [CrossRef]
107. Vučković, S.; Samela, J.; Nordlund, K.; Popok, V.N. Pinning of size-selected Co clusters on highly ordered pyrolytic graphite. *Eur. Phys. J. D* **2009**, *52*, 107–110. [CrossRef]
108. Popok, V.N.; Vučković, S.; Samela, J.; Järvi, T.T.; Nordlund, K.; Campbell, E.E.B. Stopping of energetic cobalt clusters and formation of radiation damage in graphite. *Phys. Rev. B* **2009**, *80*, 205419. [CrossRef]
109. Smith, R.; Nock, C.; Kenny, S.; BelBruno, J.J.; Di Vece, M.; Palomba, S.; Palmer, R.E. Modeling the pinning of Au and Ni clusters on graphite. *Phys. Rev. B* **2006**, *73*, 125429. [CrossRef]
110. Smith, R.; Kenny, S.; BelBruno, J.; Palmer, R. Chapter 15 Modelling the structure and dynamics of metal nanoclusters deposited on graphite. In *Atomic Clusters: From Gas Phase to Deposition*; Woodruff, D.P., Ed.; Elsevier: Amsterdam, The Netherlands, 2007; pp. 589–616.
111. Convers, P.; Monot, R.; Harbich, W.; Seminara, L. Implantation of size-selected silver clusters into graphite. *Eur. Phys. J. D* **2004**, *29*, 49–56. [CrossRef]
112. Samela, J.; Nordlund, K.; Keinonen, J.; Popok, V.N.; Campbell, E.E.B. Argon cluster impacts on layered silicon, silica, and graphite surfaces. *Eur. Phys. J. D* **2007**, *43*, 181–184. [CrossRef]
113. Chang, H.; Bard, A.J. Scanning tunneling microscopy studies of carbon-oxygen reactions on highly oriented pyrolytic graphite. *J. Am. Chem. Soc.* **1991**, *113*, 5588–5596. [CrossRef]
114. Datta, S.S.; Strachan, D.R.; Khamis, S.M.; Johnson, A.T.C. Crystallographic etching of few-layer graphene. *Nano Lett.* **2008**, *8*, 1912–1915. [CrossRef] [PubMed]
115. Severin, N.; Kirstein, S.; Sokolov, I.M.; Rabe, J.P. Rapid trench channeling of graphenes with catalytic silver nanoparticles. *Nano Lett.* **2009**, *9*, 457–461. [CrossRef] [PubMed]
116. Sigmund, P. Mechanisms and theory of physical sputtering by particle impact. *Nucl. Instum. Meth. Phys. Res. B* **1987**, *27*, 1–20. [CrossRef]
117. Nastasi, M.; Mayer, J.W. *Ion Implantation and Synthesis of Materials*; Springer: Berlin, Germany, 2006. [CrossRef]
118. Wilson, I.H.; Zheng, N.J.; Knipping, U.; Tsong, I.S.T. Effects of isolated atomic collision cascades on SiO2/Si interfaces studied by scanning tunneling microscopy. *Phys. Rev. B* **1988**, *38*, 8444–8450. [CrossRef]
119. Neumann, R. Scanning probe microscopy of ion-irradiated materials. *Nucl. Instrum. Methods Phys. Res. B* **1999**, *151*, 42–55. [CrossRef]
120. Colla, T.J.; Aderjan, R.; Kissel, R.; Urbassek, H.M. Sputtering of Au (111) induced by 16-keV Au cluster bombardment: Spikes, craters, late emission, and fluctuations. *Phys. Rev. B* **2000**, *62*, 8487–8493. [CrossRef]
121. Bräuchle, G.; Richard-Schneider, S.; Illig, D.; Rockenberger, J.; Beck, R.D.; Kappes, M.M. Etching nanometer sized holes of variable depth from carbon cluster impact induced defects on graphite surfaces. *Appl. Phys. Lett.* **1995**, *67*, 52–54. [CrossRef]
122. Seki, T.; Aoki, T.; Tanomura, M.; Matsuo, J.; Yamada, I. Energy dependence of a single trace created by C60 ion impact. *Mater. Chem. Phys.* **1998**, *54*, 143–146. [CrossRef]
123. Allen, L.P.; Insepov, Z.; Fenner, D.B.; Santeufemio, C.; Brooks, W.; Jones, K.S.; Yamada, I. Craters on silicon surfaces created by gas cluster ion impacts. *J. Appl. Phys.* **2002**, *92*, 3671–3678. [CrossRef]
124. Popok, V.N.; Prasalovich, S.; Campbell, E.E.B. Complex crater formation on silicon surfaces by low-energy Arn+ cluster ion implantation. *Surf. Sci.* **2004**, *566*, 1179–1184. [CrossRef]
125. Popok, V.N.; Prasalovich, S.; Campbell, E.E.B. Surface nanostructuring by implantation of cluster ions. *Vacuum* **2004**, *76*, 265–272. [CrossRef]
126. Samela, J.; Nordlund, K.; Keinonen, J.; Popok, V.N. Comparison of silicon potentials for cluster bombardment simulations. *Nucl. Instrum. Methods Phys. Res. B* **2007**, *255*, 253–258. [CrossRef]
127. Samela, J.; Nordlund, K.; Popok, V.N.; Campbell, E.E.B. Origin of complex impact craters on native oxide coated silicon surfaces. *Phys. Rev. B* **2008**, *77*, 075309. [CrossRef]

128. Prasalovich, S.; Popok, V.N.; Persson, P.O.; Campbell, E.E.B. Experimental studies of complex crater formation under cluster implantation of solids. *Eur. Phys. J. D* **2005**, *36*, 79–88. [CrossRef]
129. Popok, V.N.; Jensen, J.; Vuckovic, S.; Macková, A.; Trautmann, C. Formation of surface nanostructures on rutile (TiO_2): Comparative study of low-energy cluster ion and high-energy monoatomic ion impact. *J. Phys. D Appl. Phys.* **2009**, *42*, 205303. [CrossRef]
130. Yamaguchi, Y.; Gspann, J. Large-scale molecular dynamics simulations of cluster impact and erosion processes on a diamond surface. *Phys. Rev. B* **2002**, *66*, 155408. [CrossRef]
131. Djurabekova, F.; Samela, J.; Timko, H.; Nordlund, K.; Calatroni, S.; Taborelli, M.; Wuensch, W. Crater formation by single ions, cluster ions and ion showers. *Nucl. Instrum. Methods Phys. Res. B* **2012**, *272*, 374–376. [CrossRef]
132. Popok, V.N.; Samela, J.; Nordlund, K.; Popov, V.P. Impact of keV-energy argon clusters on diamond and graphite. *Nucl. Instrum. Methods Phys. Res. B* **2012**, *282*, 112–115. [CrossRef]
133. Popok, V.N.; Samela, J.; Nordlund, K.; Campbell, E.E.B. Stopping of energetic argon cluster ions in graphite: Role of cluster momentum and charge. *Phys. Rev. B* **2010**, *82*, 201403. [CrossRef]
134. Gruber, A. Nanoparticle impact micromachining. *J. Vac. Sci. Technol. B* **1997**, *15*, 2362. [CrossRef]
135. Popok, V.N.; Prasalovich, S.; Campbell, E.E.B. Nanohillock formation by impact of small low-energy clusters with surfaces. *Nucl. Instrum. Methods Phys. Res. B* **2003**, *207*, 145–153. [CrossRef]
136. Cleveland, C.L.; Landman, U. Dynamics of cluster-surface collisions. *Science* **1992**, *257*, 355–361. [CrossRef]
137. Melosh, H.J.; Ivanov, B.A. Impact crater collapse. *Annu. Rev. Earth Planet. Sci.* **1999**, *27*, 385–415. [CrossRef]
138. Yamada, I. Materials processing by gas cluster ion beams. *Mater. Sci. Eng. R Rep.* **2001**, *34*, 231–295. [CrossRef]
139. Nazarov, A.V.; Chernysh, V.; Nordlund, K.; Djurabekova, F.; Zhao, J. Spatial distribution of particles sputtered from single crystals by gas cluster ions. *Nucl. Instrum. Methods Phys. Res. B* **2017**, *406*, 518–522. [CrossRef]
140. Matsuo, J.; Toyoda, N.; Akizuki, M.; Yamada, I. Sputtering of elemental metals by Ar cluster ions. *Nucl. Instrum. Methods Phys. Res. B* **1997**, *121*, 459–463. [CrossRef]
141. Toyoda, N.; Yamada, I. Size effects of gas cluster ions on beam transport, amorphous layer formation and sputtering. *Nucl. Instrum. Methods Phys. Res. B* **2009**, *267*, 1415–1419. [CrossRef]
142. Winograd, N. The magic of cluster SIMS. *Anal. Chem.* **2005**, *77*, 142 A–149 A. [CrossRef]
143. Gilmore, I. SIMS of organics—Advances in 2D and 3D imaging and future outlook. *J. Vac. Sci. Technol. A* **2013**, *31*, 050819. [CrossRef]
144. Shard, A.G.; Havelund, R.; Seah, M.P.; Spencer, S.J.; Gilmore, I.; Winograd, N.; Mao, D.; Miyayama, T.; Niehuis, E.; Rading, D.; et al. Argon cluster ion beams for organic depth profiling: Results from a VAMAS interlaboratory study. *Anal. Chem.* **2012**, *84*, 7865–7873. [CrossRef]
145. Seah, M.P.; Gilmore, I. Cluster primary ion sputtering: Correlations in secondary ion intensities in TOF SIMS. *Surf. Interface Anal.* **2010**, *43*, 228–235. [CrossRef]
146. Angerer, T.B.; Blenkinsopp, P.; Fletcher, J.S. High energy gas cluster ions for organic and biological analysis by time-of-flight secondary ion mass spectrometry. *Int. J. Mass Spectrom.* **2015**, *377*, 591–598. [CrossRef]
147. Paruch, R.J.; Garrison, B.J.; Mlynek, M.; Postawa, Z. On universality in sputtering yields due to cluster bombardment. *J. Phys. Chem. Lett.* **2014**, *5*, 3227–3230. [CrossRef]
148. Averback, R.; Ghaly, M. MD studies of the interactions of low energy particles and clusters with surfaces. *Nucl. Instrum. Methods Phys. Res. B* **1994**, *90*, 191–201. [CrossRef]
149. Yamamura, Y. Sputtering by cluster ions. *Nucl. Instrum. Methods Phys. Res. B* **1988**, *33*, 493–496. [CrossRef]
150. Shulga, V.; Sigmund, P. Penetration of slow gold clusters through silicon. *Nucl. Instrum. Methods Phys. Res. B* **1990**, *47*, 236–242. [CrossRef]
151. Shulga, V.I.; Vicanek, M.; Sigmund, P. Pronounced nonlinear behavior of atomic collision sequences induced by keV-energy heavy ions in solids and molecules. *Phys. Rev. A* **1989**, *39*, 3360–3372. [CrossRef] [PubMed]
152. Ravagnan, L.; Divitini, G.; Rebasti, S.; Marelli, M.; Piseri, P.; Milani, P. Poly(methyl methacrylate)-palladium clusters nanocomposite formation by supersonic cluster beam deposition: A method for microstructured metallization of polymer surfaces. *J. Phys. D Appl. Phys.* **2009**, *42*, 082002. [CrossRef]
153. Cardia, R.; Melis, C.; Colombo, L. Neutral-cluster implantation in polymers by computer experiments. *J. Appl. Phys.* **2013**, *113*, 224307. [CrossRef]
154. Ziegler, J.F.; Ziegler, M.; Biersack, J. SRIM—The stopping and range of ions in matter (2010). *Nucl. Instrum. Methods Phys. Res. B* **2010**, *268*, 1818–1823. [CrossRef]

155. Möller, W.; Eckstein, W.; Biersack, J. Tridyn-binary collision simulation of atomic collisions and dynamic composition changes in solids. *Comput. Phys. Commun.* **1988**, *51*, 355–368. [CrossRef]
156. Toyoda, N.; Yamada, I. Gas cluster ion beam equipment and applications for surface processing. *IEEE Trans. Plasma Sci.* **2008**, *36*, 1471–1488. [CrossRef]
157. Gilmer, G.; Roland, C.; Stock, D.; Jaraíz, M.; De La Rubia, T.D. Simulations of thin film deposition from atomic and cluster beams. *Mater. Sci. Eng. B* **1996**, *37*, 1–7. [CrossRef]
158. Anders, C.; Urbassek, H.M. Cluster-size dependence of ranges of 100eV/atom Aun clusters. *Nucl. Instrum. Methods Phys. Res. B* **2005**, *228*, 57–63. [CrossRef]
159. Pratontep, S.; Preece, P.; Xirouchaki, C.; Palmer, R.E.; Sanz-Navarro, C.; Kenny, S.; Smith, R. Scaling relations for implantation of size-selected Au, Ag, and Si clusters into graphite. *Phys. Rev. Lett.* **2003**, *90*, 55503. [CrossRef]
160. Popok, V.N.; Samela, J.; Nordlund, K.; Popov, V.P. Implantation of keV-energy argon clusters and radiation damage in diamond. *Phys. Rev. B* **2012**, *85*, 033405. [CrossRef]
161. Tyo, E.C.; Vajda, S. Catalysis by clusters with precise numbers of atoms. *Nat. Nanotechnol.* **2015**, *10*, 577–588. [CrossRef] [PubMed]
162. Heiz, U.; Bullock, E.L. Fundamental aspects of catalysis on supported metal clusters. *J. Mater. Chem.* **2004**, *14*, 564–577. [CrossRef]
163. Bansmann, J.; Baker, S.; Binns, C.; Blackman, J.; Bucher, J.-P.; Dorantesdavila, J.; Dupuis, V.; Favre, L.; Kechrakos, D.; Kleibert, A. Magnetic and structural properties of isolated and assembled clusters. *Surf. Sci. Rep.* **2005**, *56*, 189–275. [CrossRef]
164. Benel, C.; Reisinger, T.; Kruk, R.; Hahn, H. Cluster-assembled nanocomposites: Functional properties by design. *Adv. Mater.* **2018**, *31*, 1806634. [CrossRef] [PubMed]
165. Kreibig, U.; Volmer, M. Optics of nanosized metals. In *Handbook of Optical Properties: Optics of Small Particles, Interfaces, and Surfaces*; Hummel, R.E., Wissman, P., Eds.; CRC Press: Boca Raton, FL, USA, 1997; Volume 2, pp. 145–190.
166. Pelton, M.; Aizpurua, J.; Bryant, G. Metal-nanoparticle plasmonics. *Laser Photon. Rev.* **2008**, *2*, 136–159. [CrossRef]
167. Halas, N.J.; Lal, S.; Chang, W.-S.; Link, S.; Nordlander, P. Plasmons in strongly coupled metallic nanostructures. *Chem. Rev.* **2011**, *111*, 3913–3961. [CrossRef] [PubMed]
168. Jeon, T.Y.; Park, S.-G.; Kim, S.-H.; Kim, D.J.; Kim, D.-H. Nanostructured plasmonic substrates for use as SERS sensors. *Nano Converg.* **2016**, *3*, 2957. [CrossRef]
169. Ghisleri, C.; Siano, M.; Ravagnan, L.; Potenza, M.A.C.; Milani, P. Nanocomposite-based stretchable optics. *Laser Photon. Rev.* **2013**, *7*, 1020–1026. [CrossRef]
170. Marom, S.; Dorresteijn, M.; Modi, R.; Podesta, A.; Di Vece, M. Silver nanoparticles from a gas aggregation nanoparticle source for plasmonic efficiency enhancement in a-Si solar cells. *Mater. Res. Express* **2019**, *6*, 045012. [CrossRef]
171. Minnai, C.; Bellacicca, A.; Brown, S.A.; Milani, P. Facile fabrication of complex networks of memristive devices. *Sci. Rep.* **2017**, *7*, 7955. [CrossRef]
172. Santaniello, T.; Milani, P. Additive nano-manufacturing of 3D printed electronics using supersonic cluster beam deposition. *Front. Nanosci.* **2020**, *15*, 313–333. [CrossRef]
173. Santaniello, T.; Migliorini, L.; Yan, Y.; Lenardi, C.; Milani, P. Supersonic cluster beam fabrication of metal–ionogel nanocomposites for soft robotics. *J. Nanopart. Res.* **2018**, *20*, 250. [CrossRef]
174. Fostner, S.; Nande, A.; Smith, A.; Gazoni, R.M.; Grigg, J.; Temst, K.; Van Bael, M.J.; Brown, S.A. Percolating transport in superconducting nanoparticle films. *J. Appl. Phys.* **2017**, *122*, 223905. [CrossRef]
175. Zheng, M.; Li, W.; Xu, M.; Xu, N.; Chen, P.; Han, M.; Xie, B. Strain sensors based on chromium nanoparticle arrays. *Nanoscale* **2014**, *6*, 3930–3933. [CrossRef] [PubMed]
176. Li, S.; Lin, M.M.; Toprak, M.S.; Kim, K.; Muhammed, M. Nanocomposites of polymer and inorganic nanoparticles for optical and magnetic applications. *Nano Rev.* **2010**, *1*, 5214. [CrossRef]
177. Kim, J.; Van Der Bruggen, B. The use of nanoparticles in polymeric and ceramic membrane structures: Review of manufacturing procedures and performance improvement for water treatment. *Environ. Pollut.* **2010**, *158*, 2335–2349. [CrossRef]
178. Benetti, G.; Cavaliere, E.; Banfi, F.; Gavioli, L. Antimicrobial nanostructured coatings: A gas phase deposition and magnetron sputtering perspective. *Materials* **2020**, *13*, 784. [CrossRef]

179. Kylián, O.; Popok, V.N. Applications of polymer films with gas-phase aggregated nanoparticles. *Front. Nanosci.* **2020**, *15*, 119–162. [CrossRef]
180. Meyer, R.; Lemire, C.; Shaikhutdinov, S.K.; Freund, H.-J. Surface chemistry of catalysis by gold. *Gold Bull.* **2004**, *37*, 72–124. [CrossRef]
181. Arenz, M.; Gilb, S.; Heiz, U. Size effects in the chemistry of small clusters. *Chem. Phys. Sol. Surf.* **2007**, *12*, 1–51. [CrossRef]
182. Haruta, M. Gold catalysts prepared by coprecipitation for low-temperature oxidation of hydrogen and of carbon monoxide. *J. Catal.* **1989**, *115*, 301–309. [CrossRef]
183. Castleman, A.W.; Bowen, K.H. Clusters: Structure, energetics, and dynamics of intermediate states of matter. *J. Phys. Chem.* **1996**, *100*, 12911–12944. [CrossRef]
184. Heiz, U.; Schneider, W.-D. Nanoassembled model catalysts. *J. Phys. D Appl. Phys.* **2000**, *33*, R85–R102. [CrossRef]
185. Lang, S.; Popolan, D.; Bernhardt, T. Chemical reactivity and catalytic properties of size-selected gas-phase metal clusters. *Chem. Phys. Sol. Surf.* **2007**, *12*, 53–90. [CrossRef]
186. Poppa, H. Nucleation, growth, and TEM analysis of metal particles and clusters deposited in UHV. *Catal. Rev.* **1993**, *35*, 359–398. [CrossRef]
187. Chen, M.; Goodman, D. Oxide-supported metal clusters. *Chem. Phys. Sol. Surf.* **2007**, *12*, 201–269. [CrossRef]
188. Mammen, N.; Spanu, L.; Tyo, E.C.; Yang, B.; Halder, A.; Seifert, S.; Pellin, M.J.; Vajda, S.; Narasimhan, S. Reversing size-dependent trends in the oxidation of copper clusters through support effects. *Eur. J. Inorg. Chem.* **2017**, *2018*, 16–22. [CrossRef]
189. Halder, A.; Vajda, S. Synchrotron characterization of clusters for catalysis. *Front. Nanosci.* **2020**, *15*, 1–29. [CrossRef]
190. Arenz, M.; Landman, U.; Heiz, U. CO combustion on supported gold clusters. *Chem. Phys. Chem.* **2006**, *7*, 1871–1879. [CrossRef]
191. Mayoral, A.; Martínez, L.; Garcia-Martin, J.M.; Fernández-Martinez, I.; Garcia-Hernandez, M.; Galiana, B.; Ballesteros, C.; Huttel, Y. Tuning the size, composition and structure of Au and $Co_{50}Au_{50}$ nanoparticles by high-power impulse magnetron sputtering in gas phase synthesis. *Nanotechnology* **2019**, *30*, 065606. [CrossRef]
192. Yang, B.; Liu, C.; Halder, A.; Tyo, E.C.; Martinson, A.B.F.; Seifert, S.; Zapol, P.; Curtiss, L.A.; Vajda, S. Copper cluster size effect in methanol synthesis from CO2. *J. Phys. Chem. C* **2017**, *121*, 10406–10412. [CrossRef]
193. Chen, P.-T.; Tyo, E.C.; Hayashi, M.; Pellin, M.J.; Safonova, O.V.; Nachtegaal, M.; Van Bokhoven, J.A.; Vajda, S.; Zapol, P. Size-selective reactivity of subnanometer Ag4 and Ag16 clusters on a TiO2 surface. *J. Phys. Chem. C* **2017**, *121*, 6614–6625. [CrossRef]
194. Gawande, M.B.; Goswami, A.; Asefa, T.; Guo, H.; Biradar, A.V.; Peng, D.-L.; Zbořil, R.; Varma, R. Core–shell nanoparticles: Synthesis and applications in catalysis and electrocatalysis. *Chem. Soc. Rev.* **2015**, *44*, 7540–7590. [CrossRef] [PubMed]
195. Jang, M.-H.; Kizilkaya, O.; Kropf, A.J.; Kurtz, R.L.; Elam, J.W.; Lei, Y. Synergetic effect on catalytic activity and charge transfer in Pt-Pd bimetallic model catalysts prepared by atomic layer deposition. *J. Chem. Phys.* **2020**, *152*, 024710. [CrossRef] [PubMed]
196. Raja, R.; Hermans, S.; Shephard, D.S.; Johnson, B.F.G.; Sankar, G.; Bromley, S.T.; Thomas, J.M. Preparation and characterisation of a highly active bimetallic (Pd–Ru) nanoparticle heterogeneous catalyst†. *Chem. Commun.* **1999**, 1571–1572. [CrossRef]
197. Negreiros, F.R.; Halder, A.; Yin, C.; Singh, A.; Barcaro, G.; Sementa, L.; Tyo, E.C.; Pellin, M.J.; Bartling, S.; Meiwes-Broer, K.-H.; et al. Bimetallic Ag-Pt sub-nanometer supported clusters as highly efficient and robust oxidation catalysts. *Angew. Chem. Int. Ed.* **2017**, *57*, 1209–1213. [CrossRef]
198. Roy, C.; Sebok, B.; Scott, S.B.; Fiordaliso, E.M.; Sørensen, J.E.; Bodin, A.; Trimarco, D.B.; Damsgaard, C.D.; Vesborg, P.C.K.; Hansen, O.; et al. Impact of nanoparticle size and lattice oxygen on water oxidation on NiFeOxHy. *Nat. Catal.* **2018**, *1*, 820–829. [CrossRef]
199. Bodin, A.; Christoffersen, A.-L.N.; Elkjær, C.F.; Brorson, M.; Kibsgaard, J.; Helveg, S.; Chorkendorff, I. Engineering Ni–Mo–S nanoparticles for hydrodesulfurization. *Nano Lett.* **2018**, *18*, 3454–3460. [CrossRef]
200. Guirado-López, R.A.; Dorantes-Dávila, J.; Pastor, G.M. Orbital magnetism in transition-metal clusters: From hund's rules to bulk quenching. *Phys. Rev. Lett.* **2003**, *90*, 226402. [CrossRef]
201. Peredkov, S.; Neeb, M.; Eberhardt, W.; Meyer, J.; Tombers, M.; Kampschulte, H.; Niedner-Schatteburg, G. Spin and orbital magnetic moments of free nanoparticles. *Phys. Rev. Lett.* **2011**, *107*, 233401. [CrossRef]

202. Cox, A.J.; Louderback, J.G.; Apsel, S.E.; Bloomfield, L.A. Magnetism in 4d-transition metal clusters. *Phys. Rev. B* **1994**, *49*, 12295–12298. [CrossRef] [PubMed]
203. Payne, F.W.; Jiang, W.; Bloomfield, L.A. Magnetism and magnetic isomers in free chromium clusters. *Phys. Rev. Lett.* **2006**, *97*, 193401. [CrossRef] [PubMed]
204. Binns, C.; Blackman, J. Magnetism in isolated clusters. In *Metallic Nanoparticles*; Blackman, J.A., Ed.; Elsevier: Amsterdam, The Netherlands, 2008; pp. 231–275. [CrossRef]
205. Bucher, J.-P.; Khanna, S.N. Magnetism of free and supported metal clusters. In *Quantum Phenomena in Clusters and Nanostructures*; Khanna, S.N., Castleman, A.W., Jr., Eds.; Springer: Berlin, Germany, 2003; pp. 83–137. [CrossRef]
206. Martins, M.; Wurth, W. Magnetic properties of supported metal atoms and clusters. *J. Phys. Condens. Matter* **2016**, *28*, 503002. [CrossRef]
207. Mukherjee, P.; Manchanda, P.; Kumar, P.; Zhou, L.; Kramer, M.J.; Arti, K.; Skomski, R.; Sellmyer, D.; Shield, J.E. Size-induced chemical and magnetic ordering in individual Fe–Au nanoparticles. *ACS Nano* **2014**, *8*, 8113–8120. [CrossRef] [PubMed]
208. Koten, M.A.; Mukherjee, P.; Shield, J.E. Core-shell nanoparticles driven by surface energy differences in the Co-Ag, W-Fe, and Mo-Co systems. *Part. Part. Syst. Charact.* **2015**, *32*, 848–853. [CrossRef]
209. Rui, X.; Shield, J.E.; Sun, Z.; Xu, Y.; Sellmyer, D.J. In-cluster-structured exchange-coupled magnets with high energy densities. *Appl. Phys. Lett.* **2006**, *89*, 122509. [CrossRef]
210. Kharchenko, A.; Lukashevich, M.; Popok, V.N.; Khaibullin, R.; Valeev, V.; Bazarov, V.; Petracic, O.; Wieck, A.D.; Odzhaev, V. Correlation of electronic and magnetic properties of thin polymer layers with cobalt nanoparticles. *Part. Part. Syst. Charact.* **2013**, *30*, 180–184. [CrossRef]
211. Koch, S.A.; Palasantzas, G.; Vystavel, T.; De Hosson, J.T.M.; Binns, C.; Louch, S. Magnetic and structural properties of Co nanocluster thin films. *Phys. Rev. B* **2005**, *71*, 085410. [CrossRef]
212. Zare-Kolsaraki, H.; Hackenbroich, B.; Micklitz, H. Strongly enhanced tunneling magnetoresistance in granular films of Co clusters in a CO 2 matrix: Evidence for a cluster-surface/matrix interaction. *Europhys. Lett.* **2002**, *57*, 866–871. [CrossRef]
213. Binns, C.; Maher, M.J.; Pankhurst, Q.A.; Kechrakos, D.; Trohidou, K.N. Magnetic behavior of nanostructured films assembled from preformed Fe clusters embedded in Ag. *Phys. Rev. B* **2002**, *66*, 184413. [CrossRef]
214. Katz, E.; Willner, I. Integrated nanoparticle-biomolecule hybrid systems: Synthesis, properties, and applications. *Angew. Chem. Int. Ed.* **2004**, *43*, 6042–6108. [CrossRef]
215. Schmelzer, J.W.P.; Brown, S.A.; Wurl, A.; Hyslop, M.; Blaikie, R.J. Finite-size effects in the conductivity of cluster assembled nanostructures. *Phys. Rev. Lett.* **2002**, *88*, 226802. [CrossRef] [PubMed]
216. Lassesson, A.; Schulze, M.; Van Lith, J.; Brown, S.A. Tin oxide nanocluster hydrogen and ammonia sensors. *Nanotechnology* **2007**, *19*, 015502. [CrossRef] [PubMed]
217. Xie, B.; Liu, L.; Peng, X.; Zhang, Y.; Xu, Q.; Zheng, M.; Takiya, T.; Han, M. Optimizing hydrogen sensing behavior by controlling the coverage in Pd nanoparticle films. *J. Phys. Chem. C* **2011**, *115*, 16161–16166. [CrossRef]
218. Barborini, E.; Vinati, S.; Leccardi, M.; Repetto, P.; Bertolini, G.; Rorato, O.; Lorenzelli, L.; DeCarli, M.; Guarnieri, V.; Ducati, C.; et al. Batch fabrication of metal oxide sensors on micro-hotplates. *J. Micromech. Microeng.* **2008**, *18*, 55015. [CrossRef]
219. Chen, M.; Luo, W.; Xu, Z.; Zhang, X.; Xie, B.; Wang, G.; Han, M. An ultrahigh resolution pressure sensor based on percolative metal nanoparticle arrays. *Nat. Commun.* **2019**, *10*, 4024–4029. [CrossRef]
220. Langer, J.; Novikov, S.M.; Liz-Marzán, L.M. Sensing using plasmonic nanostructures and nanoparticles. *Nanotechnology* **2015**, *26*, 322001. [CrossRef]
221. Gong, Y.; Zhou, Y.; He, L.; Xie, B.; Song, F.; Han, M.; Wang, G. Systemically tuning the surface plasmon resonance of high-density silver nanoparticle films. *Eur. Phys. J. D* **2013**, *67*, 87. [CrossRef]
222. Novikov, S.M.; Popok, V.N.; Evlyukhin, A.B.; Muhammad, H.; Morgen, P.; Fiutowski, J.; Beermann, J.; Rubahn, H.-G.; Bozhevolnyi, S.I. Highly stable monocrystalline silver clusters for plasmonic applications. *Langmuir* **2017**, *33*, 6062–6070. [CrossRef]
223. Popok, V.N.; Novikov, S.M.; Lebedinskij, Y.Y.; Markeev, A.M.; Andreev, A.A.; Trunkin, I.N.; Arsenin, A.V.; Volkov, V.S. Gas-aggregated copper nanoparticles with long-term plasmon resonance stability. *Plasmonics* **2020**, in press. [CrossRef]

224. Polonskyi, O.; Kylián, O.; Drabik, M.; Kousal, J.; Solar, P.; Artemenko, A.; Čechvala, J.; Choukourov, A.; Slavinska, D.; Biederman, H. Deposition of Al nanoparticles and their nanocomposites using a gas aggregation cluster source. *J. Mater. Sci.* **2014**, *49*, 3352–3360. [CrossRef]
225. Minnai, C.; Milani, P. Metal-polymer nanocomposite with stable plasmonic tuning under cyclic strain conditions. *Appl. Phys. Lett.* **2015**, *107*, 73106. [CrossRef]
226. Karas, M.; Bachmann, D.; Hillenkamp, F. Influence of the wavelength in high-irradiance ultraviolet laser desorption mass spectrometry of organic molecules. *Anal. Chem.* **1985**, *57*, 2935–2939. [CrossRef]
227. Tanaka, K.; Waki, H.; Ido, Y.; Akita, S.; Yoshida, Y.; Yoshida, T.; Matsuo, T. Protein and polymer analyses up tom/z 100 000 by laser ionization time-of-flight mass spectrometry. *Rapid Commun. Mass Spectrom.* **1988**, *2*, 151–153. [CrossRef]
228. Hillenkamp, F.; Karas, M.; Beavis, R.C.; Chait, B.T. Matrix-assisted laser desorption/ionization mass spectrometry of biopolymers. *Anal. Chem.* **1991**, *63*, 1193A–1203A. [CrossRef] [PubMed]
229. Karas, M.; Krüger, R. Ion formation in MALDI: The cluster ionization mechanism. *Chem. Rev.* **2003**, *103*, 427–440. [CrossRef] [PubMed]
230. Dreisewerd, K. Recent methodological advances in MALDI mass spectrometry. *Anal. Bioanal. Chem.* **2014**, *406*, 2261–2278. [CrossRef] [PubMed]
231. Chen, C.-H. Mass spectrometry for forensic applications. In *Encyclopedia of Analytical Chemistry*; John Wiley & Sons: Chichester, UK, 2000; pp. 1–15. [CrossRef]
232. Brodbelt, J.S.; Hildenbrand, Z.L.; Schug, K.A. Applications of MALDI-TOF MS in environmental microbiology. *Analyst* **2016**, *141*, 2827–2837. [CrossRef]
233. Duncan, M.W.; Nedelkov, D.; Walsh, R.; Hattan, S.J. Applications of MALDI mass spectrometry in clinical chemistry. *Clin. Chem.* **2016**, *62*, 134–143. [CrossRef]
234. Seng, P.; Rolain, J.-M.; Fournier, P.-E.; La Scola, B.; Drancourt, M.; Raoult, D. MALDI-TOF-mass spectrometry applications in clinical microbiology. *Future Microbiol.* **2010**, *5*, 1733–1754. [CrossRef]
235. Croxatto, A.; Prod'Hom, G.; Greub, G. Applications of MALDI-TOF mass spectrometry in clinical diagnostic microbiology. *FEMS Microbiol. Rev.* **2012**, *36*, 380–407. [CrossRef] [PubMed]
236. Pavlovic, M.; Huber, I.; Konrad, R.; Busch, U. Application of MALDI-TOF MS for the identification of food borne bacteria. *Open Microbiol. J.* **2013**, *7*, 135–141. [CrossRef] [PubMed]
237. Parker, C.E.; Pearson, T.W.; Anderson, N.L.; Borchers, C.H. Mass-spectrometry-based clinical proteomics—A review and prospective. *Analyst* **2010**, *135*, 1830–1838. [CrossRef] [PubMed]
238. Cleland, T.P.; Schroeter, E.R. A comparison of common mass spectrometry approaches for paleoproteomics. *J. Proteome Res.* **2018**, *17*, 936–945. [CrossRef]
239. Castellana, E.T.; Sherrod, S.D.; Russell, D.H. Nanoparticles for selective laser desorption/ionization in mass spectrometry. *J. Lab. Autom.* **2008**, *13*, 330–334. [CrossRef]
240. Yonezawa, T.; Kawasaki, H.; Tarui, A.; Watanabe, T.; Arakawa, R.; Shimada, T.; Mafuné, F. Detailed investigation on the possibility of nanoparticles of various metal elements for surface-assisted laser desorption/ionization mass spectrometry. *Anal. Sci.* **2009**, *25*, 339–346. [CrossRef]
241. Hayasaka, T.; Goto-Inoue, N.; Zaima, N.; Shrivas, K.; Kashiwagi, Y.; Yamamoto, M.; Nakamoto, M.; Setou, M. Imaging mass spectrometry with silver naeoparticles reveals the distribution of fatty acids in mouse retinal sections. *J. Am. Soc. Mass Spectrom.* **2010**, *21*, 1446–1454. [CrossRef]
242. Abdelhamid, H.N. Nanoparticle assisted laser desorption/ionization mass spectrometry for small molecule analytes. *Microchim. Acta* **2018**, *185*, 200. [CrossRef]
243. Ng, K.-M.; Chau, S.-L.; Tang, H.-W.; Wei, X.-G.; Lau, K.-C.; Ye, F.; Ng, A.M.C. Ion-desorption efficiency and internal-energy transfer in surface-assisted laser desorption/ionization: More implication(s) for the thermal-driven and phase-transition-driven desorption process. *J. Phys. Chem. C* **2015**, *119*, 23708–23720. [CrossRef]
244. Li, Y.; Cao, X.; Zhan, L.; Xue, J.; Wang, J.; Xiong, C.; Nie, Z. Hot electron transfer promotes ion production in plasmonic metal nanostructure assisted laser desorption ionization mass spectrometry. *Chem. Commun.* **2018**, *54*, 10905–10908. [CrossRef] [PubMed]
245. Prysiazhnyi, V.; Dycka, F.; Kratochvíl, J.; Stranak, V.; Popok, V.N. Effect of Ag nanoparticle size on ion formation in nanoparticle assisted LDI MS. *Appl. Nano* **2020**, *1*, 2. [CrossRef]
246. Prysiazhnyi, V.; Dycka, F.; Kratochvíl, J.; Stranak, V.; Ksirova, P.; Hubicka, Z. Silver nanoparticles for solvent-free detection of small molecules and mass-to-charge calibration of laser desorption/ionization mass spectrometry. *J. Vac. Sci. Technol. B* **2019**, *37*, 012906. [CrossRef]

247. Prysiazhnyi, V.; Dycka, F.; Kratochvil, J.; Sterba, J.; Stranak, V. Gas-aggregated Ag nanoparticles for detection of small molecules using LDI MS. *Anal. Bioanal. Chem.* **2019**, *412*, 1037–1047. [CrossRef] [PubMed]
248. Muller, L.; Kailas, A.; Jackson, S.N.; Roux, A.; Barbacci, D.C.; Schultz, J.A.; Balaban, C.D.; Woods, A.S. Lipid imaging within the normal rat kidney using silver nanoparticles by matrix-assisted laser desorption/ionization mass spectrometry. *Kidney Int.* **2015**, *88*, 186–192. [CrossRef] [PubMed]
249. Jackson, S.N.; Baldwin, K.; Muller, L.; Womack, V.M.; Schultz, J.A.; Balaban, C.D.; Woods, A.S. Imaging of lipids in rat heart by MALDI-MS with silver nanoparticles. *Anal. Bioanal. Chem.* **2013**, *406*, 1377–1386. [CrossRef] [PubMed]
250. Muller, L.; Baldwin, K.; Barbacci, D.C.; Jackson, S.N.; Roux, A.; Balaban, C.D.; Brinson, B.E.; McCully, M.I.; Lewis, E.K.; Schultz, J.A.; et al. Laser desorption/ionization mass spectrometric imaging of endogenous lipids from rat brain tissue implanted with silver nanoparticles. *J. Am. Soc. Mass Spectrom.* **2017**, *28*, 1716–1728. [CrossRef]
251. Corbelli, G.; Ghisleri, C.; Marelli, M.; Milani, P.; Ravagnan, L. Highly deformable nanostructured elastomeric electrodes with improving conductivity upon cyclical stretching. *Adv. Mater.* **2011**, *23*, 4504–4508. [CrossRef]
252. Gnatkovsky, V.; Cattalini, A.; Antonini, A.; Spreafico, L.; Saini, M.; Noe, F.; Alessi, C.; Librizzi, L.; Uva, L.; Marras, C.E.; et al. Recording electrical brain activity with novel stretchable electrodes based on supersonic cluster beam implantation nanotechnology on conformable polymers. *Int. J. Nanomed.* **2019**, *14*, 10079–10089. [CrossRef]
253. Popok, V.N. Ion implantation of polymers: Formation of nanoparticulate materials. *Rev. Adv. Mater. Sci.* **2012**, *30*, 1–26.
254. Minnai, C.; Di Vece, M.; Milani, P. Mechanical-optical-electro modulation by stretching a polymer-metal nanocomposite. *Nanotechnology* **2017**, *28*, 355702. [CrossRef]
255. Potenza, M.A.C.; Nazzari, D.; Cremonesi, L.; Denti, I.; Milani, P. Hyperspectral imaging with deformable gratings fabricated with metal-elastomer nanocomposites. *Rev. Sci. Instrum.* **2017**, *88*, 113105. [CrossRef] [PubMed]
256. Aqra, F.; Ayyad, A. Surface free energy of alkali and transition metal nanoparticles. *Appl. Surf. Sci.* **2014**, *314*, 308–313. [CrossRef]
257. Ruffino, F.; Torrisi, V.; Marletta, G.; Grimaldi, M.G. Effects of the embedding kinetics on the surface nano-morphology of nano-grained Au and Ag films on PS and PMMA layers annealed above the glass transition temperature. *Appl. Phys. A* **2012**, *107*, 669–683. [CrossRef]
258. Bonde, H.C.; Fojan, P.; Popok, V.N. Controllable embedding of size-selected copper nanoparticles into polymer films. *Plasma Process. Polym.* **2020**, *17*, 1900237. [CrossRef]
259. Hanif, M.; Juluri, R.R.; Fojan, P.; Popok, V.N. Polymer films with size-selected silver nanoparticles as plasmon resonance-based transducers for protein sensing. *Biointerface Res. Appl. Chem.* **2016**, *6*, 1564–1568.
260. Popok, V.N.; Muhammad, H.; Ceynowa, F.; Fojan, P. Immersion of low-energy deposited metal clusters into poly(methyl methacrylate). *Nucl. Instrum. Methods Phys. Res. B* **2017**, *409*, 91–95. [CrossRef]
261. Ceynowa, F.A.; Chirumamilla, M.; Zenin, V.A.; Popok, V.N. Arrays of size-selected metal nanoparticles formed by cluster ion beam technique. *MRS Adv.* **2018**, *3*, 2771–2776. [CrossRef]
262. Kuzminova, A.; Beranová, J.; Polonskyi, O.; Shelemin, A.; Kylián, O.; Choukourov, A.; Slavinska, D.; Biederman, H. Antibacterial nanocomposite coatings produced by means of gas aggregation source of silver nanoparticles. *Surf. Coat. Technol.* **2016**, *294*, 225–230. [CrossRef]
263. Kylián, O.; Kratochvíl, J.; Petr, M.; Kuzminova, A.; Slavinska, D.; Biederman, H.; Beranová, J. Ag/C:F antibacterial and hydrophobic nanocomposite coatings. *Funct. Mater. Lett.* **2017**, *10*, 1750029. [CrossRef]
264. Kratochvíl, J.; Sterba, J.; Lieskovská, J.; Langhansová, H.; Kuzminova, A.; Khalakhan, I.; Kylián, O.; Stranak, V. Antibacterial effect of Cu/C:F nanocomposites deposited on PEEK substrates. *Mater. Lett.* **2018**, *230*, 96–99. [CrossRef]
265. Kratochvíl, J.; Kuzminova, A.; Kylián, O. State-of-the-art, and perspectives of, silver/plasma polymer antibacterial nanocomposites. *Antibiotics* **2018**, *7*, 78. [CrossRef] [PubMed]
266. Kylián, O.; Polonskyi, O.; Kratochvíl, J.; Artemenko, A.; Choukourov, A.; Drabik, M.; Solar, P.; Slavinska, D.; Biederman, H.; Choukourov, A. Control of wettability of plasma polymers by application of Ti nano-clusters. *Plasma Process. Polym.* **2011**, *9*, 180–187. [CrossRef]

267. Kuzminova, A.; Shelemin, A.; Kylián, O.; Petr, M.; Kratochvíl, J.; Solar, P.; Biederman, H. From super-hydrophilic to super-hydrophobic surfaces using plasma polymerization combined with gas aggregation source of nanoparticles. *Vacuum* **2014**, *110*, 58–61. [CrossRef]
268. Kylián, O.; Kuzminova, A.; Hanuš, J.; Slavinska, D.; Biederman, H. Super-hydrophilic SiOx coatings prepared by plasma enhanced chemical vapor deposition combined with gas aggregation source of nanoparticles. *Mater. Lett.* **2018**, *227*, 5–8. [CrossRef]
269. Shelemin, A.; Nikitin, D.; Choukourov, A.; Kylián, O.; Kousal, J.; Khalakhan, I.; Melnichuk, I.; Slavinska, D.; Biederman, H.; Choukourov, A. Preparation of biomimetic nano-structured films with multi-scale roughness. *J. Phys. D Appl. Phys.* **2016**, *49*, 254001. [CrossRef]
270. Choukourov, A.; Kylián, O.; Petr, M.; Vaidulych, M.; Nikitin, D.; Hanuš, J.; Artemenko, A.; Shelemin, A.; Gordeev, I.; Kolská, Z.; et al. RMS roughness-independent tuning of surface wettability by tailoring silver nanoparticles with a fluorocarbon plasma polymer. *Nanoscale* **2017**, *9*, 2616–2625. [CrossRef]
271. Kylián, O.; Petr, M.; Serov, A.; Solar, P.; Polonskyi, O.; Hanuš, J.; Choukourov, A.; Biederman, H. Hydrophobic and super-hydrophobic coatings based on nanoparticles overcoated by fluorocarbon plasma polymer. *Vacuum* **2014**, *100*, 57–60. [CrossRef]
272. Petr, M.; Hanuš, J.; Kylián, O.; Kratochvíl, J.; Solar, P.; Slavinska, D.; Biederman, H. Superhydrophobic fluorine-free hierarchical coatings produced by vacuum based method. *Mater. Lett.* **2016**, *167*, 30–33. [CrossRef]
273. Kratochvíl, J.; Kuzminova, A.; Solař, P.; Hanuš, J.; Kylián, O.; Biederman, H. Wetting and drying on gradient-nanostructured C:F surfaces synthesized using a gas aggregation source of nanoparticles combined with magnetron sputtering of polytetrafluoroethylene. *Vacuum* **2019**, *166*, 50–56. [CrossRef]
274. Vaidulych, M.; Shelemin, A.; Hanuš, J.; Khalakhan, I.; Krakovsky, I.; Kočová, P.; Mašková, H.; Kratochvíl, J.; Pleskunov, P.; Štěrba, J.; et al. Superwettable antibacterial textiles for versatile oil/water separation. *Plasma Process. Polym.* **2019**, *16*, 1900003. [CrossRef]
275. Solar, P.; Kylián, O.; Marek, A.; Vandrovcova, M.; Bačáková, L.; Hanuš, J.; Vyskocil, J.; Slavinska, D.; Biederman, H. Particles induced surface nanoroughness of titanium surface and its influence on adhesion of osteoblast-like MG-63 cells. *Appl. Surf. Sci.* **2015**, *324*, 99–105. [CrossRef]
276. Kylián, O.; Kratochvíl, J.; Hanuš, J.; Polonskyi, O.; Solař, P.; Biederman, H. Fabrication of Cu nanoclusters and their use for production of Cu/plasma polymer nanocomposite thin films. *Thin Solid Films* **2014**, *550*, 46–52. [CrossRef]
277. Vahl, A.; Carstens, N.; Strunskus, T.; Faupel, F.; Hassanien, A. Diffusive memristive switching on the nanoscale, from individual nanoparticles towards scalable nanocomposite devices. *Sci. Rep.* **2019**, *9*, 17367. [CrossRef] [PubMed]
278. Polonskyi, O.; Solar, P.; Kylián, O.; Drabik, M.; Artemenko, A.; Kousal, J.; Hanuš, J.; Pešička, J.; Matolínová, I.; Kolíbalová, E.; et al. Nanocomposite metal/plasma polymer films prepared by means of gas aggregation cluster source. *Thin Solid Films* **2012**, *520*, 4155–4162. [CrossRef]
279. Maicu, M.; Schmittgens, R.; Hecker, D.; Glöß, D.; Frach, P.; Gerlach, G. Synthesis and deposition of metal nanoparticles by gas condensation process. *J. Vac. Sci. Technol. A* **2014**, *32*, 2. [CrossRef]
280. Hanuš, J.; Steinhartová, T.; Kylián, O.; Kousal, J.; Malinský, P.; Choukourov, A.; Macková, A.; Biederman, H. Deposition of Cu/a-C:H nanocomposite films. *Plasma Process. Polym.* **2016**, *13*, 879–887. [CrossRef]
281. Vaidulych, M.; Hanuš, J.; Steinhartová, T.; Kylián, O.; Choukourov, A.; Beranová, J.; Khalakhan, I.; Biederman, H. Deposition of Ag/a-C:H nanocomposite films with Ag surface enrichment. *Plasma Process. Polym.* **2017**, *14*, 1600256. [CrossRef]
282. Thukkaram, M.; Vaidulych, M.; Kylián, O.; Hanus, J.; Rigole, P.; Aliakbarshirazi, S.; Asadian, M.; Nikiforov, A.; Van Tongel, A.; Biederman, H.; et al. Investigation of Ag/a-C:H nanocomposite coatings on titanium for orthopedic applications. *ACS Appl. Mater. Interfaces* **2020**, *12*, 23655–23666. [CrossRef]
283. Zeng, H.; Du, X.; Singh, S.C.; Kulinich, S.A.; Yang, S.; He, J.; Cai, W. Nanomaterials via laser ablation/irradiation in liquid: A review. *Adv. Funct. Mater.* **2012**, *22*, 1333–1353. [CrossRef]
284. Streubel, R.; Barcikowski, S.; Gökce, B. Continuous multigram nanoparticle synthesis by high-power, high-repetition-rate ultrafast laser ablation in liquids. *Opt. Lett.* **2016**, *41*, 1486–1489. [CrossRef]
285. Sportelli, M.C.; Izzi, M.; Volpe, A.; Clemente, M.; Picca, R.A.; Ancona, A.; Lugarà, P.M.; Palazzo, G.; Cioffi, N.; Izzi, M. The pros and cons of the use of laser ablation synthesis for the production of silver nano-antimicrobials. *Antibiotics* **2018**, *7*, 67. [CrossRef] [PubMed]

286. Premkumar, P.A.; Starostin, S.A.; De Vries, H.; Paffen, R.M.J.; Creatore, M.; Eijkemans, T.J.; Koenraad, P.M.; Van De Sanden, M. High quality SiO2-like layers by large area atmospheric pressure plasma enhanced CVD: Deposition process studies by surface analysis. *Plasma Process. Polym.* **2009**, *6*, 693–702. [CrossRef]
287. Ding, Y.; Yamada, R.; Gresback, R.; Zhou, S.; Pi, X.; Nozaki, T. A parametric study of non-thermal plasma synthesis of silicon nanoparticles from a chlorinated precursor. *J. Phys. D Appl. Phys.* **2014**, *47*, 485202. [CrossRef]
288. Bilik, N.; Greenberg, B.L.; Yang, J.; Aydil, E.S.; Kortshagen, U.R. Atmospheric-pressure glow plasma synthesis of plasmonic and photoluminescent zinc oxide nanocrystals. *J. Appl. Phys.* **2016**, *119*, 243302. [CrossRef]
289. Mariotti, D.; Sankaran, R.M. Microplasmas for nanomaterials synthesis. *J. Phys. D Appl. Phys.* **2010**, *43*, 323001. [CrossRef]
290. Yu, W.; Xie, H. A review on nanofluids: Preparation, stability mechanisms, and applications. *J. Nanomater.* **2012**, *2012*, 435873. [CrossRef]
291. Taylor, R.A.; Coulombe, S.; Otanicar, T.; Phelan, P.; Gunawan, A.; Lv, W.; Rosengarten, G.; Prasher, R.; Tyagi, H. Small particles, big impacts: A review of the diverse applications of nanofluids. *J. Appl. Phys.* **2013**, *113*, 011301. [CrossRef]

© 2020 by the authors. Licensee MDPI, Basel, Switzerland. This article is an open access article distributed under the terms and conditions of the Creative Commons Attribution (CC BY) license (http://creativecommons.org/licenses/by/4.0/).